MEX3B leads to aberrant expression of VCAN, aggravating the thoracic aortic dissection by contributing to the phenotype transformation of VSMCs

JIANMAO HONG*, BIJUN XU*, SHIQIANG WANG and FAN HE

Department of Cardiac Surgery, Sir Run Run Shaw Hospital, School of Medicine, Zhejiang University, Hangzhou, Zhejiang 310016, P.R. China

Received January 28, 2026; Accepted September 9, 2026

DOI: 10.3892/ijmm.2026.6044

Abstract. Thoracic aortic dissection (TAD) is a lethal condition due to the risk of aortic rupture and malperfusion of arterial branches. Currently, effective treatments are unavailable due to the unclear pathogenic mechanisms; therefore, it is essential to explore the underlying mechanisms of TAD to find novel therapeutic targets. The present study aimed to explore the effects of Mex3 RNA-binding family member B (MEX3B) on TAD pathogenesis. A murine model of TAD was established with β-aminopropionitrile monofumarate and angiotensin II. Hematoxylin and eosin and elastic Van Gieson staining were performed to assess the TAD formation and fragmentation of elastic fibers. Echocardiography was applied to measure the diameter of thoracic aorta. RT-qPCR, western blot, and immunohistochemistry were employed to detect the expression of phenotypic transformation markers of vascular smooth muscle cells (VSMCs). mRNA sequencing was performed to further explore the downstream factors of MEX3B. MEX3B was upregulated following TAD induction. Knockdown of MEX3B alleviated TAD formation, as evidenced by decreased diameter and hematomas of thoracic aorta, as well as the enhanced integrity of the aortic structure and decreased thrombi in the false lumens. Loss of MEX3B mitigated the TAD-induced depletion and fragmentation of elastic fibers. *In vitro*, small interfering RNA pool-mediated MEX3B downregulation triggered VSMC switching from a synthetic towards a contractile phenotype. High-throughput transcriptomics demonstrated that the MEX3B knockdown reduced the expression of versican (VCAN). MEX3B potentiated VCAN mRNA stability by binding to its 3'untranslated region. VCAN downregulation induced a contractile phenotype of VSMCs. In conclusion, the loss of MEX3B protected against TAD, potentially via its contribution to VSMC phenotype switching, which may be associated with the downregulation of VCAN. The present study preliminarily demonstrated the function and mechanism of MEX3B in TAD. These findings provide a theoretical basis for understanding TAD pathogenesis.

Correspondence to: Dr Fan He, Department of Cardiac Surgery, Sir Run Run Shaw Hospital, School of Medicine, Zhejiang University, 3 Qingchun East Road, Shangcheng, Hangzhou, Zhejiang 310016, P.R. China
E-mail: 3322050@zju.edu.cn

*Contributed equally

Key words: thoracic aortic dissection, Mex3 RNA-binding family member B, vascular smooth muscle cell, versican, RNA-binding protein

Introduction

Thoracic aortic dissection (TAD) is defined as the tearing of aortic intima leading to the separation of the aortic wall layers, followed by the false lumen of aortic media (1). The rapid progression of the condition and its high incidence during the acute phase of TAD are the main clinical characteristics of TAD (2). The annual incidence of TAD is ~7.6 cases/100,000 individuals, and the mortality caused by TAD rupture is up to 80% among patients who are not diagnosed and treated quickly (3-5). Endovascular stent graft implantation or open surgical repair is used for the therapy for TAD (6). Certain patients with TAD experience persistent aortic degeneration that needs further pharmacotherapeutic intervention, however, few options are available as the molecular mechanisms of TAD remain unclear. Thus, it is essential to explore the underlying mechanisms and cell processes involved, and find novel non-invasive treatments beyond surgical repair.

The aortic media consists of vascular smooth muscle cells (VSMCs) as well as extracellular matrix, dysfunction of which is a common histological characteristic of TAD (7). Extracellular matrix in the aorta consists predominantly of elastin (ELN) and collagen, which maintain vascular wall stiffness and elasticity (8). Quantification of matrix metalloproteinase (MMP)2 and MMP9 is routinely performed to assess the degree of matrix proteolysis, as these enzymes are the key degradative agents. Several layers of VSMCs are the main source of the aorta medial layer with contractile and synthetic phenotypes. The former features low proliferative and migratory ability and high levels of contractile genes (9). By contrast, the latter is characterized by the potentiated

proliferation and migration, as well as the upregulation of genes associated with the synthesis phenotype, such as osteopontin (OPN) (9). The transformation between the two phenotypes is key for the structure and function homeostasis of aorta (10). A deeper understanding of VSMC phenotype switch is needed to provide directions to develop treatment for TAD.

Genetic information stored in chromosomal DNA is translated into protein by mRNA. This process is subject to post-transcriptional regulation, highlighting the important role of RNA-binding proteins (11). RNA-binding proteins exhibit functions in multiple steps of RNA biology, including splicing, stability and translation. RNA-binding proteins are associated with the cardiovascular system (12,13), highlighting the potential of RNA-binding proteins as a therapeutic strategy for TAD. However, it remains unknown whether dysregulation of a specific RNA-binding protein contributes to the phenotypic switching of VSMCs or the breakdown of the medial layer, two hallmark events in TAD progression.

Mex3 RNA-binding family member B (MEX3B) is a member of the muscle excess 3 protein family that binds RNA through two KH domains (14), and is an oncogenic factor (15). MEX3B is involved in the differentiation of neural progenitor cells and the silencing of MEX3B decreases expression of neural proliferation markers of neuronal progenitors (16). MEX3B knockdown (KD) alleviates murine allergic airway inflammation (17), indicating it may serve a role in the progression of TAD.

The present study aimed to investigate the effects of MEX3B on TAD progression. The β-aminopropionitrile monofumarate (BAPN) and angiotensin (Ang) II used in the murine TAD model is highly relevant to human pathogenesis because it recapitulates two key, interconnected pathological processes underlying human TAD: Extracellular matrix weakness and hemodynamic stress (18). BAPN is an irreversible inhibitor of lysyl oxidase, an enzyme essential for the cross-linking of collagen and ELN in the extracellular matrix (19). By inhibiting lysyl oxidase, BAPN disrupts the structural integrity of the aortic wall, rendering it more susceptible to mechanical stress and tear propagation. Ang II acts primarily through Ang II type 1 receptors to induce systemic hypertension, oxidative stress, inflammation and upregulation of MMPs (20). These effects lead to degradation of extracellular matrix components, VSMC phenotypic switching and weakening of the medial layer of the aorta (20). The combined effect of BAPN and Ang II results in the formation and propagation of an intimal tear, culminating in TAD (18). In the present study, VSMCs were assessed in an *in vitro* model. Next, mRNA sequencing (seq) was performed to further explore the downstream factors of MEX3B.

Materials and methods

Animal experiments. All animal experiments were approved by The Laboratory Animal Welfare and Ethics Review Committee of Zhejiang University (Hangzhou, China) following The Guideline for the Care and Use of Laboratory Animals (approval no. 29060). C57BL/6J male mice were obtained from HFK Bioscience and housed with food and water *ad libitum* at 22±1˚C and 40-60% humidity under a 12/12 h light-dark cycle (lights on at 7.00 am). Mice were randomly assigned to one of four groups: Sham, TAD, TAD + negative control (NC) or TAD + MEX3B KD. The TAD model was established by administration of BAPN (Shanghai Aladdin Biochemical Technology Co., Ltd.) and Ang II [GL Biochem (Shanghai) Ltd.] as previously described (18). Mice (age, 3 weeks, 9 g) were fed a normal diet and water containing 1 g/kg/day BAPN for 4 weeks. Osmotic mini pumps administering 1 μg/kg/min Ang II were implanted subcutaneously after anesthetization with isoflurane (induction, 3.0%; maintenance dose, 1.5%). At 24 h after implanting the micro-osmotic pumps, mice underwent echocardiography to measure the maximum diameter of the aorta under anesthesia with isoflurane. For sham group, mice were fed a normal diet and water for 4 weeks, followed by the infusion of physiological saline via micro-osmotic pumps. Mice were euthanized with 70% vol/min CO_2. Following euthanasia, cardiac and respiratory arrest, as well as fixed and dilated pupils, were observed in the mice for ~10 min to confirm death. Humane endpoints were as follows: a) sustained weight loss exceeding 20% of baseline; b) Impaired mobility or inability to access food or water autonomously; c) Signs of severe distress or pain unrelieved by analgesia; d) Clinical signs indicating severe systemic illness.

For MEX3B KD, short hairpin RNA (shRNA) targeting MEX3B or NC was synthesized by General Bio Co., Ltd. and inserted into adeno-associated virus subtype 9 (AAV9) vectors (Takara Bio Inc.). AAV-293 cells (Cellverse Bioscience Technology Co., Ltd.) were co-transfected with 7 μg of AAV transfer plasmid (MEX3B KD or NC), 14 μg pHelper (Takara Bio Inc.), and 7 μg pRC9 (Takara Bio Inc.) using Lipo3000 (Invitrogen; Thermo Fisher Scientific, Inc.) according to the manufacturer's instructions. Following incubation for 72 h at 37˚C, the cells were lysed to generate the AAV9 particles. The sequences of shRNA targeting MEX3B or NC were as follows: MEX3B, sense: 5'-GGGACAGACCACTATCCA AGT-3' and anti-sense: 5'-ACTTGGATAGTGGTCTGT CCC-3'; NC, sense: 5'-TTCTCCGAACGTGTCACGT-3' and anti-sense: 5'-ACGTGACACGTTCGGAGAA-3'. The AAV9 particles ($8x10^{11}$ viral genome/ml; 200 μl) were intravenously injected into the tail, followed by TAD induction after 3 days, as previously described (21). A double-blind method was used.

There were 88 mice: 12 mice for RNA-seq and 76 for subsequent experiments. For RNA-seq, in the sham group, aortic tissue from 5 mice were used for hematoxylin and eosin (H&E) staining. In the TAD group, 7 mice were initially enrolled; 2 died during the experiments and 2 were excluded because they did not develop TAD, indicating modeling failure. Thus, 3 mice were available for H&E staining and RNA-seq. For the subsequent experiments, the sham group consisted of 12 mice. The TAD and TAD + NC group each had 22 mice, while the TAD + MEX3B KD group had 20 mice. In the sham group, 6 mice were used for reverse transcription-quantitative (RT-q) PCR and western blot analysis and 6 were used for echocardiography followed by fixation for immunohistochemistry, immunofluorescence and pathological staining. In the TAD group, 4 mice died and 4 were excluded due to failure of TAD, leaving 14 mice; among these, 2 were used for pilot studies, 6 were used for RT-qPCR/western blotting and 6 were fixed for pathological examination. In the TAD + NC group, 5 died and 4 were excluded due to failure of TAD, leaving 13 mice, of which one was used for pilot studies, 6 for RT-qPCR/western

Table I. Sequences of siRNA targeting MEX3B or VCAN.

siRNA	Sense, 5'→3'	Antisense, 5'→3'
MEX3B siRNA 1	CCAAAGGCGCCACAAUCAATT	UUGAUUGUGGCGCCUUUGGTT
MEX3B siRNA 2	GCAUCAUUGAGCUCACAGATT	UCUGUGAGCUCAAUGAUGCTT
MEX3B siRNA 3	CAAUAACAAUAACGGCAAUTT	AUUGCCGUUAUUGUUAUUGTT
VCAN siRNA 1	GAGCAUCUUAUGGAUGUGUTT	ACACAUCCAUAAGAUGCUCTT
VCAN siRNA 2	GUGAAUUUCUCCGCAUCAATT	UUGAUGCGGAGAAAUUCACTT
VCAN siRNA 3	GUAGGCUGUUAUGGAGAUATT	UAUCUCCAUAACAGCCUACTT
Negative control	UUCUCCGAACGUGUCACGUTT	ACGUGACACGUUCGGAGAATT

si, small interfering; MEX3B, mex-3 RNA binding family member B; VCAN, versican.

blotting and 6 for pathological examination. In the TAD + KD group, 3 died and 5 were excluded due to failure of TAD, leaving 12 mice, with 6 for RT-qPCR/western blotting and 6 for pathological examination.

In total, 14 mice died spontaneously. These mice were found dead in their cages without prior signs of prolonged distress. Upon autopsy, all mice presented with massive blood clots in the thoracic cavity, confirming rupture of the dissected aorta as the direct cause of death; aortic rupture is a well-documented and inherent complication of this model (22-25).

Cell culture and transfection. Human VSMCs isolated from thoracic aortic tissue were obtained from Procell Life Science & Technology Co., Ltd. (cat. no. CP-H081). Cells were cultured with iCell primary smooth muscle cell culture system (iCell Bioscience Inc.) under 5% CO_2 at 37˚C. VSMCs were not contaminated by mycoplasma or other cell lines, demonstrated by STR profiling and mycoplasma detection and authentication.

A small interfering RNA (siRNA) pool with three siRNAs targeting MEX3B or versican (VCAN) was synthesized by JTS Scientific and transfected into VSMCs using Lipo3000 (Invitrogen; Thermo Fisher Scientific, Inc.) according to the manufacturer's instructions. Briefly, cells were incubated with 75 pmol siRNA, 250 μl Opti-MEM and 7.5 μl lipo3000 at 37˚C. After 24 h, VSMCs were treated with 100 nM Ang II for 48 h. The sequences of siRNAs targeting MEX3B or VCAN are listed in Table I. For the detection of VCAN mRNA expression, transfected VSMCs were treated with 10 μg/ml actinomycin D for 0, 4, 8 and 12 h at 37˚C prior to RT-qPCR.

Bioinformatics analysis. The data of MEX3A/MEX3B expression in aortic tissues of patients with TAD or normal samples was obtained from the National Center for Biotechnology Information (NBCI) Gene Expression Omnibus (GEO) database (accession no. GSE241265) (26,27). GSM7720285-GSM7720287 were regarded as the TAD group and GSM7720288-GSM7720290 were regarded as the control group.

RNA-seq and RT-qPCR. TRIpure Reagent (BioTeke Corporation; cat. no. RP1001) was employed to obtain the total RNA of aortic tissue or VSMCs following the manufacturer's protocols. RNA-seq was performed by Novegene Bioinform Technology Co., Ltd. RNA integrity was assessed using the Agilent 5400 Fragment Analyzer system (Agilent Technologies). Libraries were sequenced on the Illumina Novaseq X Plus platform (Illumina, Inc.) in paired-end mode with a read length of 150 bp (PE150). Sequencing was performed using the Novaseq X series 25B Reagent Kit (300 cycles; cat. no. 20104706; Illumina, Inc.). The loading concentration of the final library was 4 pM, as determined by qPCR. Transcriptome reads from RNA-seq were mapped to the reference genome (hg38 and mm39) (28,29). Data were analyzed using R v4.3.2 (r-project.org/) and org.Hs.eg.db v3.18.0 (bioconductor.org/packages/3.18/data/annotation/html/org.Hs.eg.db.html). The significance was set at $\log_2$ fold-change (FC) >1 and P<0.05. Differentially expressed genes were subjected to functional enrichment analysis by Gene Ontology (GO), Kyoto Encyclopedia of genes and genomes (KEGG) (30-32). Gene set enrichment analysis (GSEA) was performed using the GO gene sets and KEGG pathway gene sets (33). Principal component analysis (PCA) was performed to analyze the sample clustering. The RNA-seq data were uploaded to the NCBI GEO database with accession no. GSE315273.

Total mRNA was converted to cDNA using the All-in-One First-Strand SuperMix (Magen Biotechnology) according to the manufacturer's protocol. Amplification was performed using the 2X Fast Taq plus PCR Master Mix (Biosharp Life Sciences) and SYBR Green (Beijing Solarbio Science & Technology Co., Ltd.) following the manufacturers' protocols. Thermocycling conditions were as follows: Initial denaturation at 95˚C for 5 min; 40 cycles at 95˚C for 10 sec, 60˚C for 10 sec and 72˚C for 15 sec, then 72˚Cfor 90 sec, 40˚C for 1 min and a final melt at 60-90˚C (every 1˚C, 1 sec). Raw data were normalized to GAPDH, and the relative expression levels of targeted genes were calculated using $2^{-\Delta\Delta Cq}$ method (34). The sequences of primers are listed in Table II.

Western blotting. Total protein from aortic tissues or VSMCs was obtained using the RIPA lysis solution and phenylmethanesulfonyl fluoride (100:1, v/v; Beyotime Biotechnology). The concentration of protein was quantified using a BCA protein assay kit (Beyotime Biotechnology) according to the manufacturer's protocols. The proteins (20 μg/lane) were separated with 10% sodium dodecyl sulfate polyacrylamide gel electrophoresis and transferred to polyvinylidene fluoride membranes

Table II. Primer sequences for reverse transcription-quantitative PCR.

Primer	Forward, 5'→3'	Reverse, 5'→3'
mMEX3B	GCGAAGACCAACACTTACATC	CACCACGAGCCCTACCA
mMyocardin	CAGGCACCAAGACAGCG	TTGGGCGTGACAGGAAA
mCalponin 1	CAGGTCTGGGCATGGAAC	GTGGTGATTGTGGGTGGG
mOPN	CACTCCAATCGTCCCTAC	AGACTCACCGCTCTTCAT
mGAPDH	CTGCACCACCAACTGCTTAGC	CATCCACAGTCTTCTGGGTG
hMEX3B	GACCGAGTGCGTGCCAGTA	CCGTTGAGTGCCGTGTTCT
hMyocardin	ATAATACCACCACTGAAACG	GCAGTTGGAATGGACCTCT
hCalponin 1	CCACCCTCCTGGCTTTG	ATGATGTTCCGCCCTTCT
hOPN	TGCTACAGACGAGGACAT	CTATCAATCACATCGGAAT
hGAPDH	GACCTGACCTGCCGTCTAG	AGGAGTGGGTGTCGCTGT

MEX3B, mex-3 RNA binding family member B; m, mouse; OPN, osteopontin; h, human.

(Abcam). Following blocking with 1xQuickBlock Blocking Buffer (Beyotime Biotechnology) for 60 min at room temperature, proteins were incubated with the following primary antibodies: Anti-MEX3B (1:300; Santa Cruz Biotechnology, Inc.; cat. no. sc-515833), anti-VCAN (cat. no. A19655), anti-OPN (cat. no. A1361), anti-myosin heavy chain 11 (SM-MHC; all ABclonal Biotech; cat. no. A10827) and anti-GAPDH (all 1:1,000; Proteintech Group, Inc.; cat. no. 60004-1-Ig) at 4˚C overnight. Membranes were incubated with the secondary antibodies including horseradish peroxidase-conjugated goat anti-rabbit (cat. no. A0208) or anti-mouse IgG (both 1:5,000; both Beyotime Biotechnology; A0216) at 37˚C for 45 min. The bands were visualized using a BeyoECL Plus Enhanced Chemiluminescence Reagent (Beyotime Biotechnology). Strip analysis was performed using Tanon Image software version 1.10 (Tanon Science & Technology Co., Ltd.).

Pathological staining. For H&E staining, murine aortic tissue was fixed with 4% paraformaldehyde at 4˚C for 24 h, followed by embedding with paraffin and sliced into sections (5 μm). Next, the sections were deparaffinized in xylene and rehydrated in an ethanol gradient with distilled water. The sections were stained with hematoxylin for 5 min and eosin for 3 min at room temperature. The sections were observed with a BX53 light microscope (Olympus Corporation) in brightfield mode.

Elastic Van Gieson (EVG) staining was performed to visualize ELN fibers. Briefly, sections of aortic tissue were obtained as aforementioned. Then, sections were stained with Verhoeff solution and eosin at room temperature. A BX53 light microscope was used to capture the images in brightfield mode.

Immunofluorescence and immunohistochemical staining. For immunofluorescent staining, murine aortic tissue was fixed with 4% paraformaldehyde at 4˚C for 24 h, followed by embedding with paraffin and sliced into sections at a thickness of 5 μm. Next, the sections were deparaffinized in xylene and rehydrated in an ethanol gradient with distilled water. The sections were placed in boiling antigen retrieval solution and retrieved in a microwave oven at low power for 10 min. Following blocking with 1% bovine serum albumin at room temperature for 15 min, sections were incubated with primary antibodies including anti-MEX3B (1:50; Santa Cruz Biotechnology, Inc.; cat. no. Sc-515833) or anti-α-smooth muscle actin (SMA; 1:100; Cell Signaling Technology, Inc.; cat. no. 19245) at 4˚C overnight, followed by incubation with Alexa Fluor 555-conjugated anti-rabbit IgG (green) or Alexa Fluor 488-conjugated anti-mouse IgG (red; both 1:200; both Cell Signaling Technology, Inc.; cat. no. 4413 and 4408) at room temperature for 90 min away from the light. The sections were counterstained with DAPI. A BX53 fluorescence microscope was used to capture the images.

For immunohistochemical staining, murine aortic tissue was fixed with 4% paraformaldehyde at 4˚C for 24 h, followed by embedding with paraffin and then sliced into sections at a thickness of 5 μm thickness. Next, the sections were deparaffinized in xylene and rehydrated in an ethanol gradient with distilled water. The sections were placed in boiling antigen retrieval solution and retrieved in a microwave oven at low power for 10 min. After washed with phosphate buffered saline, sections were treated with 3% H_2O_2 for 15 min at room temperature and blocked with 1% bovine serum albumin at room temperature for 15 min. Then, sections were incubated with primary antibody anti-proliferating cell nuclear antigen (PCNA; 1:1,500; Proteintech Group, Inc.; cat. no. 10205-2-AP) at 4˚C overnight and secondary antibody horseradish peroxidase-conjugated goat anti-rabbit IgG (1:200; Sangon Biotech Co., Ltd.; cat. no. D110058) at room temperature for 60 min. Sections were treated with 100 μl DAB (Beijing Solarbio Science & Technology Co., Ltd.) and stained with hematoxylin (Beijing Solarbio Science & Technology Co., Ltd.; cat. no. H8070) at room temperature for 3 min. Images were captured with a BX53 light microscope in brightfield mode (magnification, x400).

VSMCs were fixed with 4% paraformaldehyde at 4˚C for 15 min and incubated with 0.1% TritonX-100 for 30 min at room temperature. Cells were washed with PBS and incubated with 1% bovine serum albumin at room temperature for 15 min. VSMCs were incubated with anti-α-SMA (1:100) at 4˚C overnight and Alexa Fluor 555 conjugated anti-rabbit IgG (1:200; both Cell Signaling Technology, Inc.; cat. no. 19245 and

4413) at room temperature for 60 min, followed by counterstaining with DAPI. Images were with captured with a BX53 fluorescence microscope (magnification, x200).

ELISA. VSMCs were centrifuged at 300 g for 10 min at 4˚C, and the supernatant was collected. The levels of MMP2, MMP9 and ELN in the supernatant of VSMCs were detected using the Human MMP2 and MMP9 (both MultiSciences Biotech; cat. nos. EK1M02 and EK1M09) and ELN ELISA kits (Wuhan Fine Biotech Co., Ltd.; cat. no. EH1505) according to the manufacturers' instructions.

Cell Counting Kit (CCK)-8. A total of $5x10^3$ VSMCs/well were seeded into the 96-well plates. Cells were treated with 10 μl CCK-8 solution (Beijing Solarbio Science & Technology Co., Ltd.) for 2 h. Absorbance was measured at 450 nm with an 800TS microplate reader (BioTek; Agilent Technologies, Inc.).

Flow cytometry. The proliferative ability of VSMCs was assessed using the E-Click EdU Cell Proliferation Flow Cytometry Assay kit (Elabscience Bionovation Inc.; cat. no. E-CK-A370) according to the manufacturer's instructions. Briefly, VSMCs were incubated with 10 μM EdU solution at 37˚C for 2 h, followed by fixation with 4% paraformaldehyde at room temperature for 15 min. Cells were washed and treated with Click solution at room temperature for 30 min, followed by detection using a NovoCyte flow cytometer (ACEA Biosciences, Inc.; Agilent Technologies, Inc.), and data analysis with NovoExpress software version 1.4.1 (ACEA Biosciences, Inc.).

Wound healing assay. VSMCs were seeded into a 6-well plate and treated with 10 μg/ml mitomycin C (Millipore Sigma) for 1 h at 37˚C. When the cells reached confluence (80%, a 200 μl pipette tip was used to create a scratch. Cells were washed with a serum-free iCell Primary Smooth Muscle Cell Culture Medium (Cellverse Bioscience Technology Co., Ltd.,) and cultured for another 24 h. The images at 0 and 24 h were captured using an IX53 light microscope. Wound closure was calculated as: (de-d)/de x100%, where de is the initial wound width at 0 h and d is the residual width at 24 h.

Transwell assay. A total of 200 μl cell suspension (within $6x10^3$ cells) resuspended in a serum-free iCell Primary Smooth Muscle Cell Culture Medium was planted into the upper chamber of a 24-well plate. VSMCs were allowed to migrate to the lower chamber, which contained 800 μl iCell Primary Smooth Muscle Cell Culture Medium with 10% fetal bovine serum (Cellverse Bioscience Technology Co., Ltd.) at 37˚C. After 24 h, VSMCs that migrated to the lower chamber were fixed with 4% paraformaldehyde at room temperature for 20 min and stained with 0.5% crystal violet (Amresco, LLC) at room temperature. The stained cells were observed with an IX53 light microscope and counted with Image J software version 1.51 j8 (National Institutes of Health).

RNA-binding protein immunoprecipitation (RIP)-PCR. A RIP assay was performed using the EZ-Magna RIP kit (MilliporeSigma (cat. no. 17-701) according to the manufacturer's protocol. In brief, cells were collected and washed with pre-cooled PBS following by centrifuging at 720 x g for 10 min at 4˚C. Then, the cells were lysed using the RIP lysis buffer. The magnetic beads were conjugated with 5 μg anti-MEX3B antibody (Santa Cruz Biotechnology, Inc.; cat. no. sc-515833) or normal mouse IgG (1:500; Beyotime Biotechnology; cat. no. A7028) at room temperature for 30 min. The cell lysates were centrifuged at 13,618 g for 10 min at 4˚C and 100 μl of supernatant was incubated with the prepped magnetic beads at 4˚C overnight. The magnetic beads were separated using a magnetic stand. Beads were digested with 18 μl of proteinase K and 15 μl of 10% sodium dodecyl sulfate at 55˚C for 30 min. The immunoprecipitated RNA was analyzed by RT-qPCR employing specific primers targeting VCAN, as aforementioned. The primers were synthesized by Beijing Solarbio Science & Technology Co., Ltd., and the sequences were as follows. Forward 5'-TGGCTTTCATAA CACTA-3'; Reverse 5'-CATTCTATCCGTCACAT-3'.

Dual-luciferase reporter assay. 293T cells (Cellverse Bioscience Technology Co., Ltd.) were planted into 12-well plates and cultured at 37˚C for 24 h. The cells were transfected with 1 μg pmirGLO (Fenghuishengwu Co., Ltd.)-VCAN 3'untranslated region (UTR) and 1 μg MEX3B overexpression or MEX3B mutKH vector using the Lipo3000 (Invitrogen; Thermo Fisher Scientific, Inc.) according to the manufacturer's protocols. MEX3B mutKH vector expresses an RNA-binding-deficient MEX3B mutant, in which key residues associated with RNA binding, including G83 and G177 in the KH domains, were replaced with D (15). After 48 h transfection at 37˚C, a dual-luciferase reporter assay was performed using Dual Luciferase Reporter Gene Assay kit (Biosharp Life Sciences) according to the manufacturer's protocols. Firefly/Renilla luminescence ratios were normalized to control.

Statistical analysis. The data were analyzed by GraphPad Prism software version 8.0 (Dotmatics) and presented as mean ± standard deviation (n=3 for the *in vitro* experiments; n=6 for the *in vivo* experiments) as previously described (21). A post hoc power analysis was conducted using G*Power 3.1.9.7 (Heinrich Heine University Düsseldorf, Düsseldorf, Germany) to evaluate the sufficiency of the sample size. Given α=0.05, n=6/group and MMP2 concentration was 4.60±0.57 ng/ml (Sham) vs. 9.57±1.56 ng/ml (TAD) vs. 10.16±1.51 ng/ml (TAD + NC) vs. 6.02±1.06 ng/ml (TAD + MEX3B KD), the power was 1.00, which exceeded the conventional threshold of 0.9. RNA-seq. The data were tested for normality test and homogeneity of variance. Unpaired Student's t-test or one-way ANOVA with post hoc Bonferroni's correction were utilized to analyze the differences. Effect size was calculated to determine the power of the analysis, as previously described (35). Student's t-tests are suitable when sample size is small and effect size is large (36,37). $P<0.05$ was considered to indicate a statistically significant difference.

Results

MEX3B is upregulated in aortic tissue of patients and mice with TAD. To understand the molecular mechanism of TAD pathogenesis, RNA-seq was performed to analyze the differentially

expressed genes in thoracic aortic tissue from TAD mice and controls. The murine TAD model was established using BAPN and Ang II (Fig. 1A). H&E staining demonstrated tearing of the aortic wall as well as formation of thrombi in the false lumens, indicating TAD formation (Fig. 1B). Total RNA from the thoracic aortic tissues was subjected to sequencing (Fig. 1C). PCA demonstrated that the samples in the TAD and sham groups were well clustered, indicating each group had a distinctive expression (Fig. 1D). There were 1,642 up- and 1,199 downregulated genes ($|\log_2 FC|>1$; $P<0.05$; Fig. 1E). Next, GSEA was performed based on GO and KEGG analysis. GO functional enrichment analysis indicated that these genes were mainly enriched in 'vascular wall composition', 'elastin catabolic process'), 'protein-RNA binding' ('protein-RNA complex organization' and 'RNA binding'), 'cell population proliferation' ('positive regulation of smooth muscle cell proliferation') and 'cell migration' (Fig. 1F). KEGG analysis by GSEA suggested that TAD was associated with 'vascular smooth muscle contraction', 'PI3K-Akt signaling pathway' and 'cytokine-cytokine receptor interaction' (Fig. 1F). These enriched terms demonstrated the potential pathogenesis of TAD.

RNA-binding proteins are key components of post-transcriptional regulatory mechanism, which are involved in numerous steps of RNA metabolism including RNA shearing, RNA stability and RNA translation (38). RNA binding proteins are associated with the cardiovascular system (13). RNA-binding proteins serve a key role in cardiovascular diseases including TAD (39,40). As RNA-seq demonstrated genes enriched in protein-RNA binding, the role of RNA binding proteins in TAD was assessed. There were 92 differently expressed genes enriched in 'protein-RNA complex organization and RNA-binding (Fig. 1G). RNA recognition motif (RRM) and the K homology (KH) domain are the most common motifs in RNA binding proteins (41). There were 15 factors with RRM domains and two with KH domains. Notably, all these factors with RRM or KH domains were upregulated in aortic tissue of TAD mice compared with the Sham group (Fig. 1H). MEX3A and MEX3B were the only two members containing KH domain. MEX3B was markedly upregulated in aortic tissue of patients with TAD according to GSE241265, whereas MEX3A was not (Fig. 1I), suggesting MEX3B may serve a role in the progression of TAD.

MEX3B KD alleviates TAD formation in vivo. To investigate the effects of MEX3B on TAD, MEX3B KD was performed via AAV9 vectors intravenously injected into mice prior to TAD induction (Fig. 2A), leading to the reversal of the MEX3B upregulation in thoracic aortic tissue of TAD mice (Fig. 2B and C). Immunofluorescence staining demonstrated that MEX3B colocalized with α-SMA in the aortic wall of mice with TAD, and the colocalization between MEX3B and α-SMA was decreased in the medial layer following AAV9 vector injection (Fig. 2D). Echocardiography demonstrated that the thoracic aorta was markedly dilated in TAD mice; this effect was reduced by MEX3B KD (Fig. 2E). The aortas of TAD mice were enlarged from the root to the thoracic segment. Hematomas were observed in the lesions, suggesting thrombosis. These pathological changes were alleviated by MEX3B KD (Fig. 2F). Next, H&E staining displayed that interfering with MEX3B expression preserved the integrity of the aortic structure and prevented the thrombi in the false lumens (Fig. 2G). EVG staining confirmed the depletion and fragmentation of elastic fibers in TAD mice, which was mitigated by MEX3B KD (Fig. 2H). The data suggested that MEX3B KD alleviates TAD formation *in vivo*.

MEX3B KD alters TAD-induced VSMC phenotype transformation in vivo. The function of MEX3B in TAD-induced VSMC phenotype transformation was explored *in vivo*. MEX3B KD reversed the TAD-induced downregulation of contractile markers myocardin and calponin 1 and upregulation of synthetic marker OPN (Fig. 3A). Loss of MEX3B upregulated the protein expression of myocardin and calponin 1 and downregulated the protein levels of OPN (Fig. 3B). MEX3B KD also upregulated the protein expression of contractile marker SM-MHC (Fig. 3B). Immunohistochemical staining demonstrated that TAD induced the upregulation of PCNA of VSMCs in the aortic medial layer, indicating the induction of the synthetic phenotype of VSMCs, while the loss of MEX3B decreased the expression of PCNA (Fig. 3C).

MEX3B KD blocks Ang II-induced VSMC phenotype switching and ELN degradation in vitro. To explore the function of MEX3B, a siRNA pool targeting MEX3B was synthesized and transfected into VSMCs, followed by the establishment of the *in vitro* model with Ang II (Fig. 4A). Ang II-induced upregulation of MEX3B was decreased in VSMCs transfected with MEX3B siRNA pools (Fig. 4B and C). The KD effects of individual siRNAs are shown in Fig. S1A: MEX3B was downregulated in VSMCs transfected with MEX3B siRNA1-3 (Fig. S1A). The mRNA expression of myocardin and calponin 1 was upregulated and OPN was downregulated in MEX3B-depleted VSMCs (Fig. 4D). Similar changes were observed in the protein expression of these factors (Fig. 4E). SM-MHC was upregulated by MEX3B KD (Fig. 4E). Immunofluorescence demonstrated that MEX3B KD reversed the downregulation of α-SMA induced by Ang II (Fig. 4F). The arterial medial layer consists of VSMCs and extracellular matrix (42). ELN and collagen are the most abundant components of extracellular matrix in the aorta and responsible for the maintenance of aortic mechanical properties (8). Changes in ELN and the degradation factors MMP2 and MMP9 were measured to investigate the degradation of extracellular matrix. The loss of MEX3B elevated ELN and decreased MMP2 and MMP9 levels (Fig. 4G). These results suggested that MEX3B KD blocks Ang II-induced VSMC phenotype switching and ELN degradation *in vitro*.

MEX3B silencing inhibits Ang II-induced phenotype transformation of VSMCs. To investigate phenotype transformation, a CCK-8 assay and EdU staining were used to assess the proliferative ability of VSMCs. Ang II-induced increased cell viability was suppressed in MEX3B KD cells (Fig. 5A). Similar proliferation inhibition was observed by EdU staining assay (Fig. 5B). Next, wound healing and Transwell assays were used to investigate the migratory ability of VSMCs.

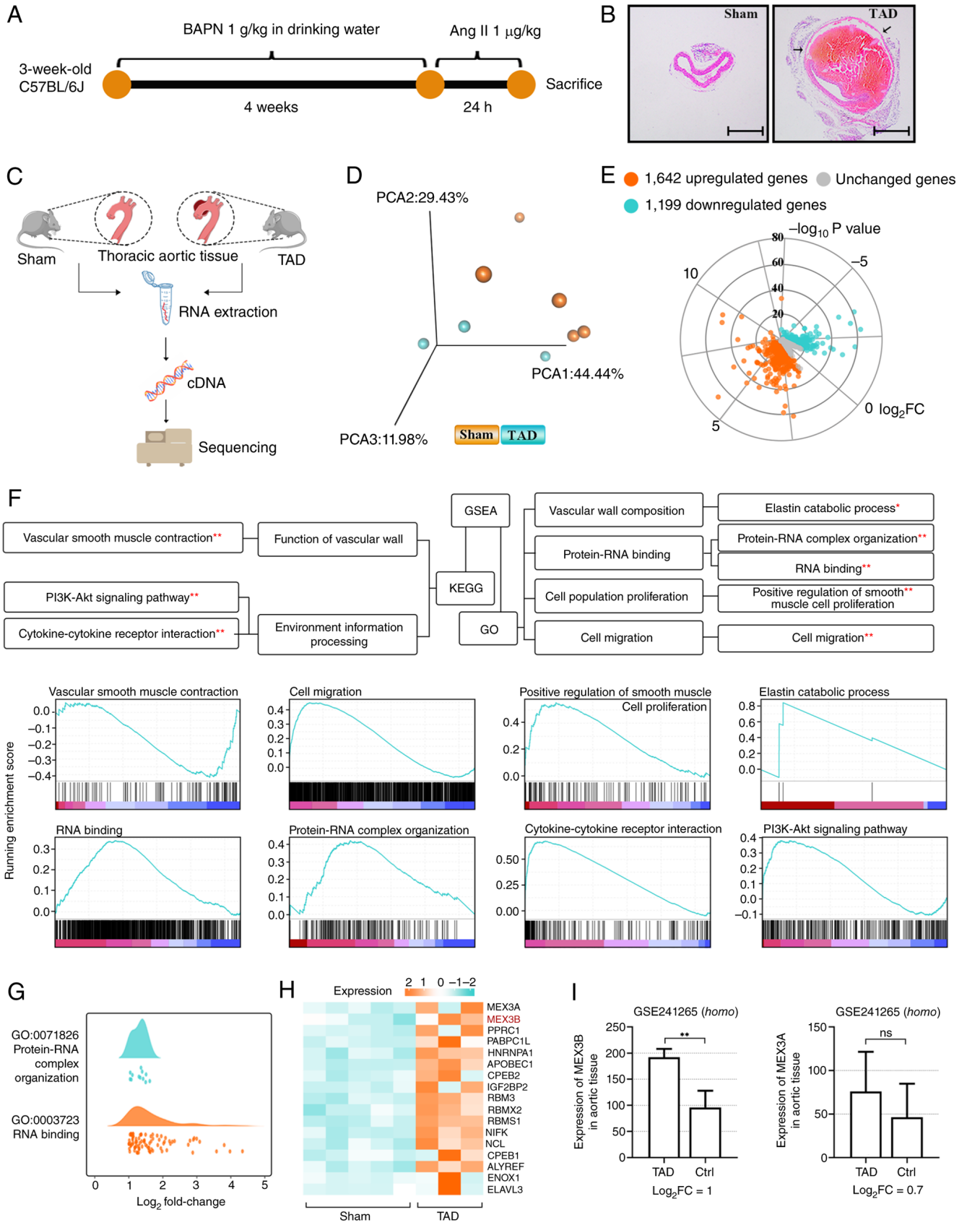


Figure 1. MEX3B is upregulated in aortic tissue of mice with TAD. (A) Timeline of TAD model induction. Murine model of TAD was established with BAPN (1 g/kg/day) for 4 weeks and Ang II (1 μg/kg) for 24 h. (B) H&E staining of thoracic aorta. Scale bar, 500 μm. Black arrows indicate the tearing of the aortic wall and formation of thrombi. (C) Sample preparation for RNA-sequencing. (D) PCA was used to identify the samples from sham and TAD group. (E) Volcano plot of differentially expressed genes ($|\log_2 FC| > 1$; $P < 0.05$). (F) GSEA. (G) Genes enriched in protein-RNA binding-associated items and their domain classification. (H) Heatmap showing the differential expression of genes with RRM and KH domains. (I) Expression of MEX3B and MEX3A in aorta tissue of patients with TAD according to the GSE241265 dataset. n=3 for TAD and n=5 for sham group. $^{*}P<0.05$; $^{**}P<0.01$. ns, not significant; Ang II, angiotensin II; BAPN, β-aminopropionitrile monofumarate; MEX3B, mex-3 RNA binding family member B; TAD, thoracic aortic dissection; PCA, principal component analysis; GSEA, gene set enrichment analysis; GO, Gene Ontology; KEGG, Kyoto Encyclopedia of Genes and Genomes.

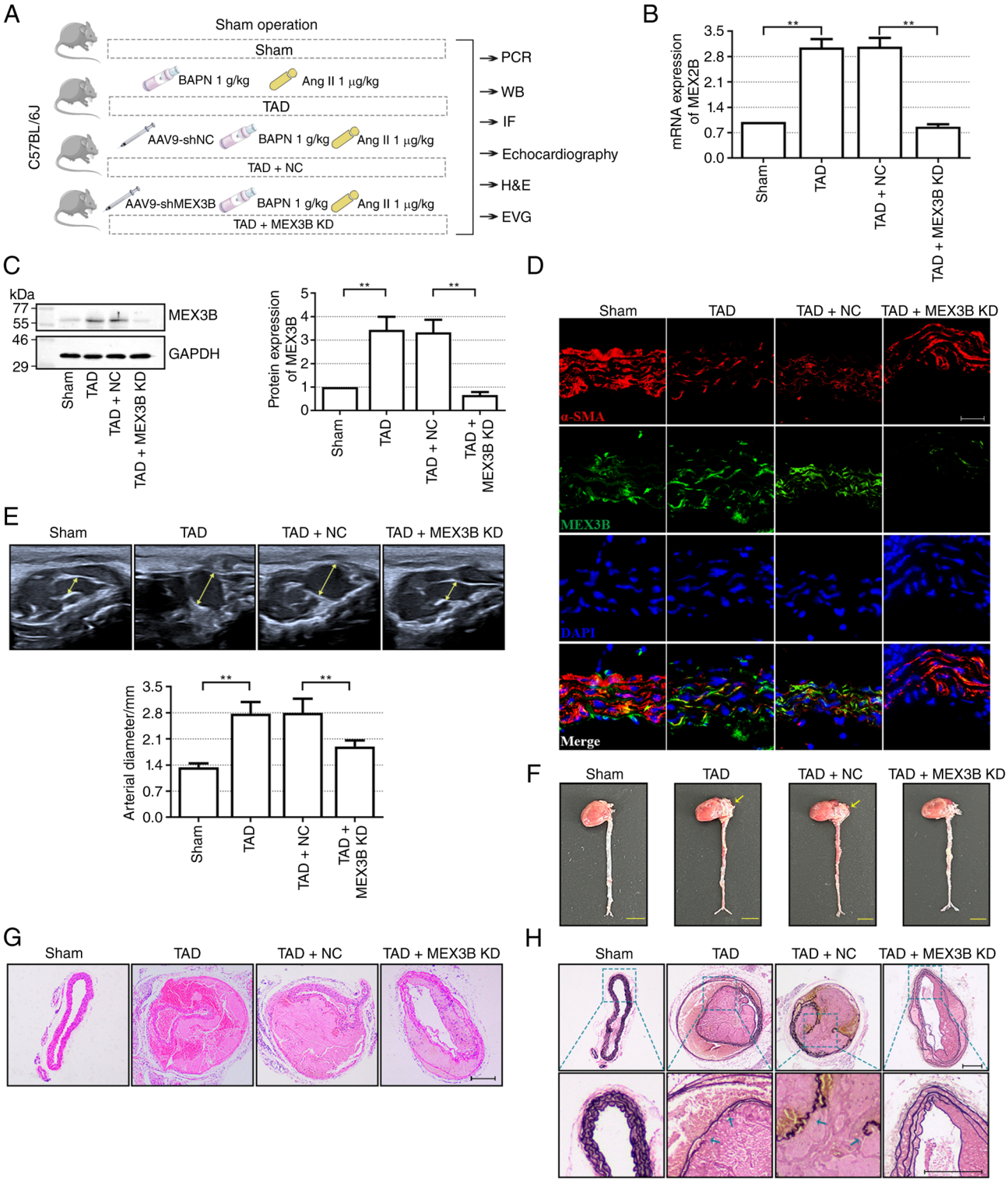


Figure 2. MEX3B knockdown improves TAD formation *in vivo*. (A) Experimental protocol. Mice were injected with $8x10^{11}$ viral genome/ml (200 μl) AAV9-shMEX3B or AAV9-shNC via tail vein, followed by TAD induction. (B) mRNA and (C) protein expression of MEX3B in the thoracic aorta tissue by WB. (D) Expression of α-SMA and MEX3B in thoracic aorta was assessed using IF staining. Scale bar, 25 μm. (E) Representative echocardiography of the maximum aortic diameter (arrow). (F) Representative gross anatomy images of the murine heart and aortic tissue. Scale bar, 0.5 cm. Yellow arrows indicate the enlargement from the root to the thoracic segment. (G) H&E staining of thoracic aorta tissue. Scale bar, 250 μm. (H) EVG staining of thoracic aorta tissue. Scale bar, 250 μm. Blue arrows indicate the elastic fiber fragmentation. n=6. **P<0.01. α-SMA, α-smooth muscle actin; MEX3B, mex-3 RNA binding family member B; TAD, thoracic aortic dissection; sh, short hairpin, NC, negative control; Ang, angiotensin; WB, western blotting; IF, immunofluorescence; H&E, hematoxylin and eosin; AAV, adeno-associated virus; EVG, elastic van Gieson; BAPN, β-aminopropionitrile monofumarate.

MEX3B KD weakened the Ang II-induced migratory ability (Fig. 5C-F). These data indicated that MEX3B KD dampens Ang II-induced phenotype switching of VSMCs.

VCAN is the downstream factor of MEX3B. RNA-seq was performed to analyze the differentially expressed genes in VSMCs with MEX3B KD in the presence of Ang II (Fig. 6A).

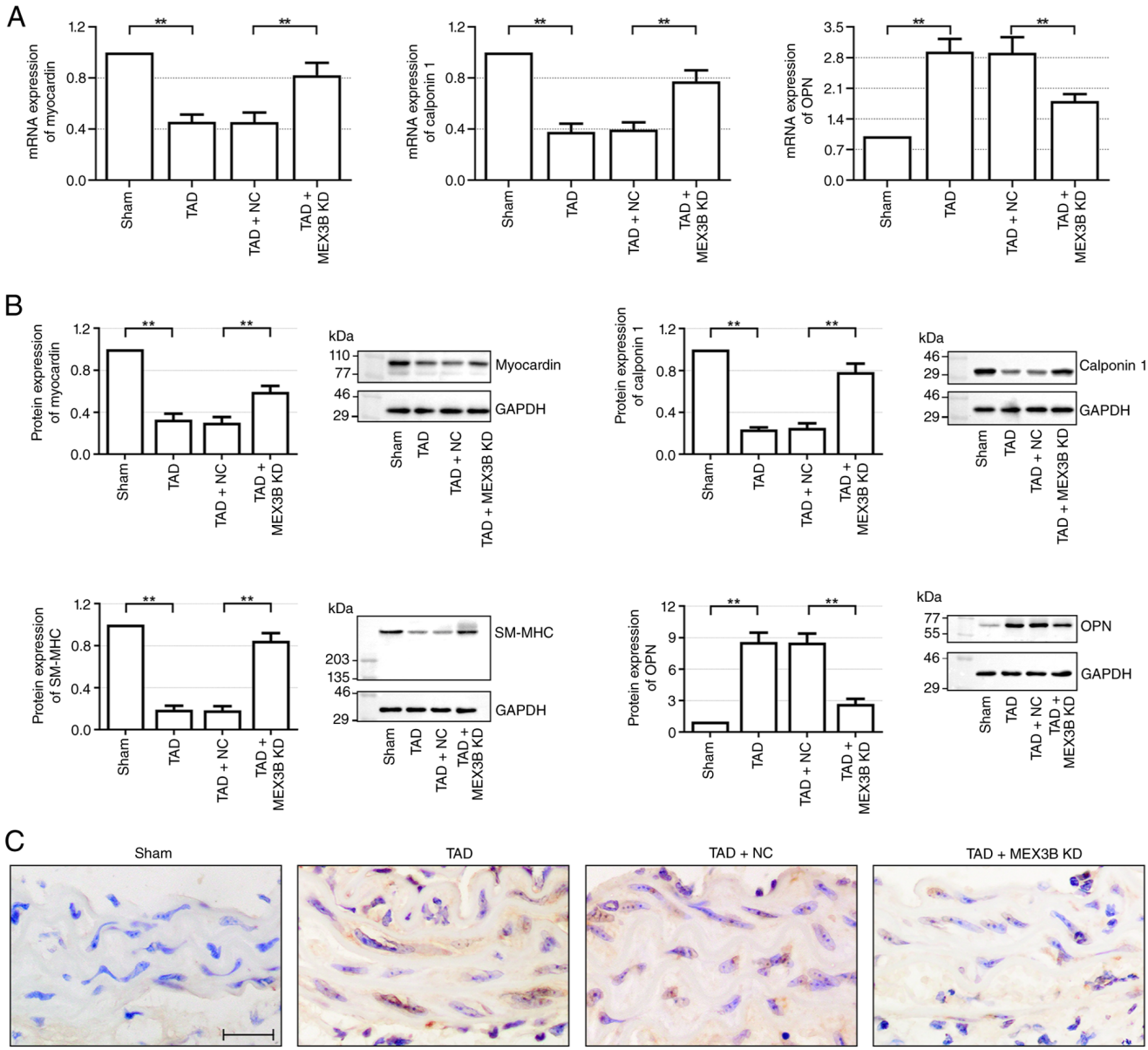


Figure 3. MEX3B KD alters TAD-induced vascular smooth muscle cell phenotypic transformation *in vivo*. (A) mRNA expression of myocardin, calponin 1 and OPN was detected by reverse transcription-quantitative PCR. (B) Protein expression of myocardin, calponin 1, SM-MHC and OPN by western blotting. (C) Expression of proliferating cell nuclear antigen was assessed using immunohistochemical staining. Scale bar, 25 μm. n=6. **P<0.01. MEX3B, mex-3 RNA binding family member B; OPN, osteopontin; SM-MHC, smooth muscle myosin heavy chain 11; TAD, thoracic aortic dissection; KD, knockdown.

PCA revealed that NC and MEX3B KD groups were well clustered in space, indicating each group had distinctive expression (Fig. 6B). There were 135 up- and 107 down-regulated genes ($|\log_2 FC|>1$; P<0.05; Fig. 6C). GO functional analysis was performed based on biological process, cellular component and molecular function. The differentially expressed genes were primarily enriched in items related to cardiovascular function. The GO items associated with the pathogenesis of TAD were screened, including 'extracellular matrix structural constituent conferring compression resistance', 'collagen-containing extracellular matrix', 'regulation of smooth muscle cell migration' and 'negative regulation of smooth muscle cell proliferation', suggesting the potential function of downstream factors of MEX3B (Fig. 6D). There were nine genes enriched in >1 pathway (Fig. 6E). VCAN is an aggregating proteoglycan, accumulation of which aggravates the TAD and the synthetic phenotype switching (43,44). In the present study, VCAN was upregulated in aortic tissue of TAD mice and downregulated in VSMCs with MEX3B KD (Fig. 6F), prompting investigation of the regulation between MEX3B and VCAN.

MEX3B potentiates VCAN mRNA stability. Consistent with the results of RNA-seq, both mRNA and protein expression of VCAN were downregulated by the loss of MEX3B (Fig. 7A). Similar results were also observed in aortic tissue of TAD mice with MEX3B KD (Fig, 7B and C). As an RNA binding protein, MEX3B regulates the mRNA stability of targets by binding to their 3'UTR. A similar mechanism between MEX3B and VCAN was confirmed by RIP-PCR assay. The RNA fragment bound to MEX3B antibody (Fig. 7D). Next, MEX3B-overexpression vectors were transfected into

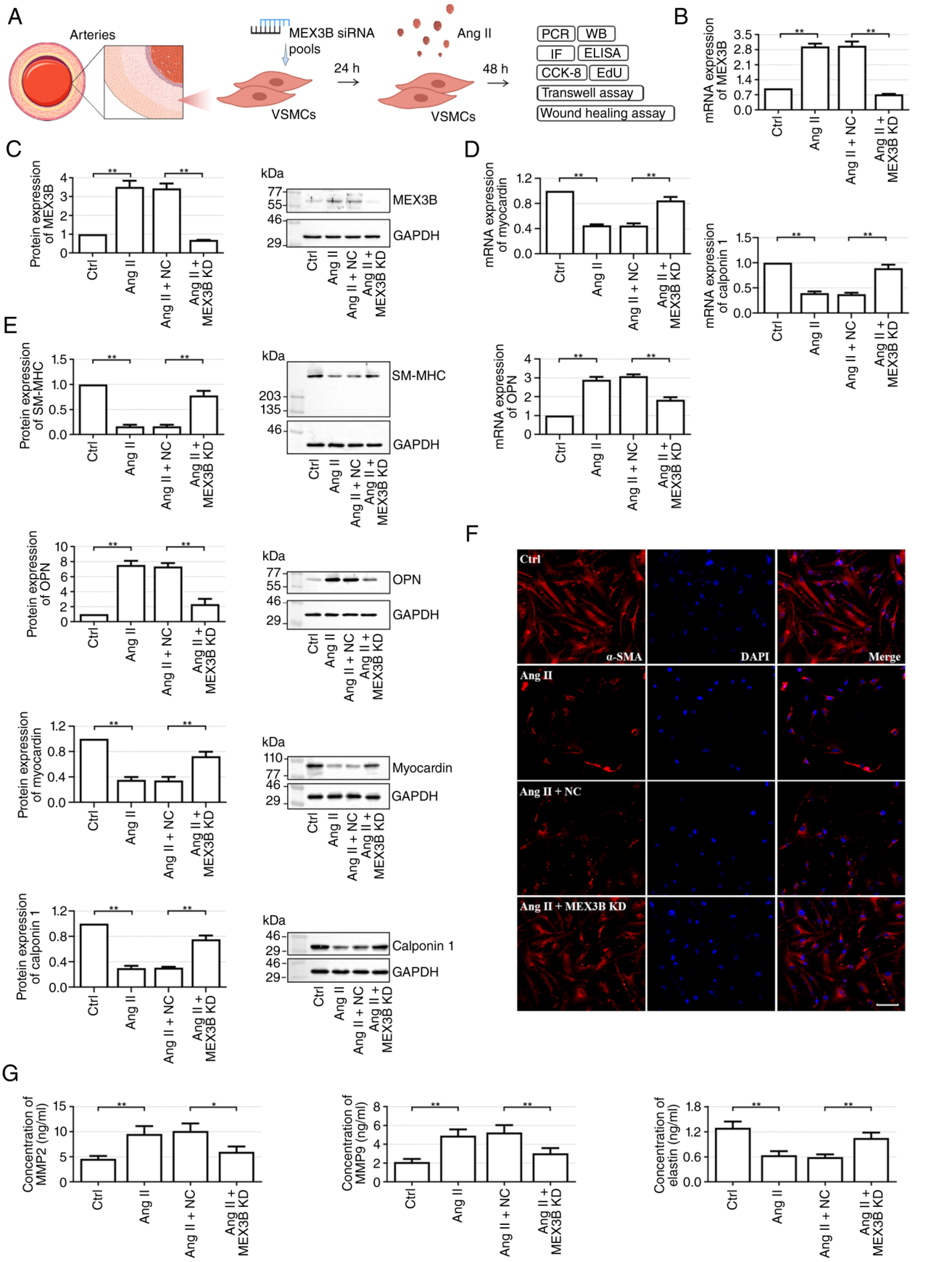


Figure 4. MEX3B KD blocks Ang II-induced VSMC phenotypic switching and elastin degradation *in vitro*. (A) Experimental protocol. VSMCs were transfected with MEX3B siRNA pools, followed by the incubation with 100 nM Ang II for 48 h. (B) mRNA and (C) protein expression of MEX3B. (D) mRNA and (E) protein expression of myocardin, calponin 1 and OPN. (F) Expression of α-SMA was assessed using IF staining. Scale bar, 100 μm. (G) Concentration of MMP2, MMP9 and elastin in cell supernatant. n=3. *P<0.05; **P<0.01. Ang II, angiotensin II; α-SMA, α-smooth muscle actin; MEX3B, mex-3 RNA binding family member B; OPN, osteopontin; SM-MHC, smooth muscle myosin heavy chain 11; VSMC, vascular smooth muscle cell; KD, knockdown; si, small interfering; Ctrl, control; WB, western blotting; IF, immunofluorescence; CCK, Cell Counting Kit.

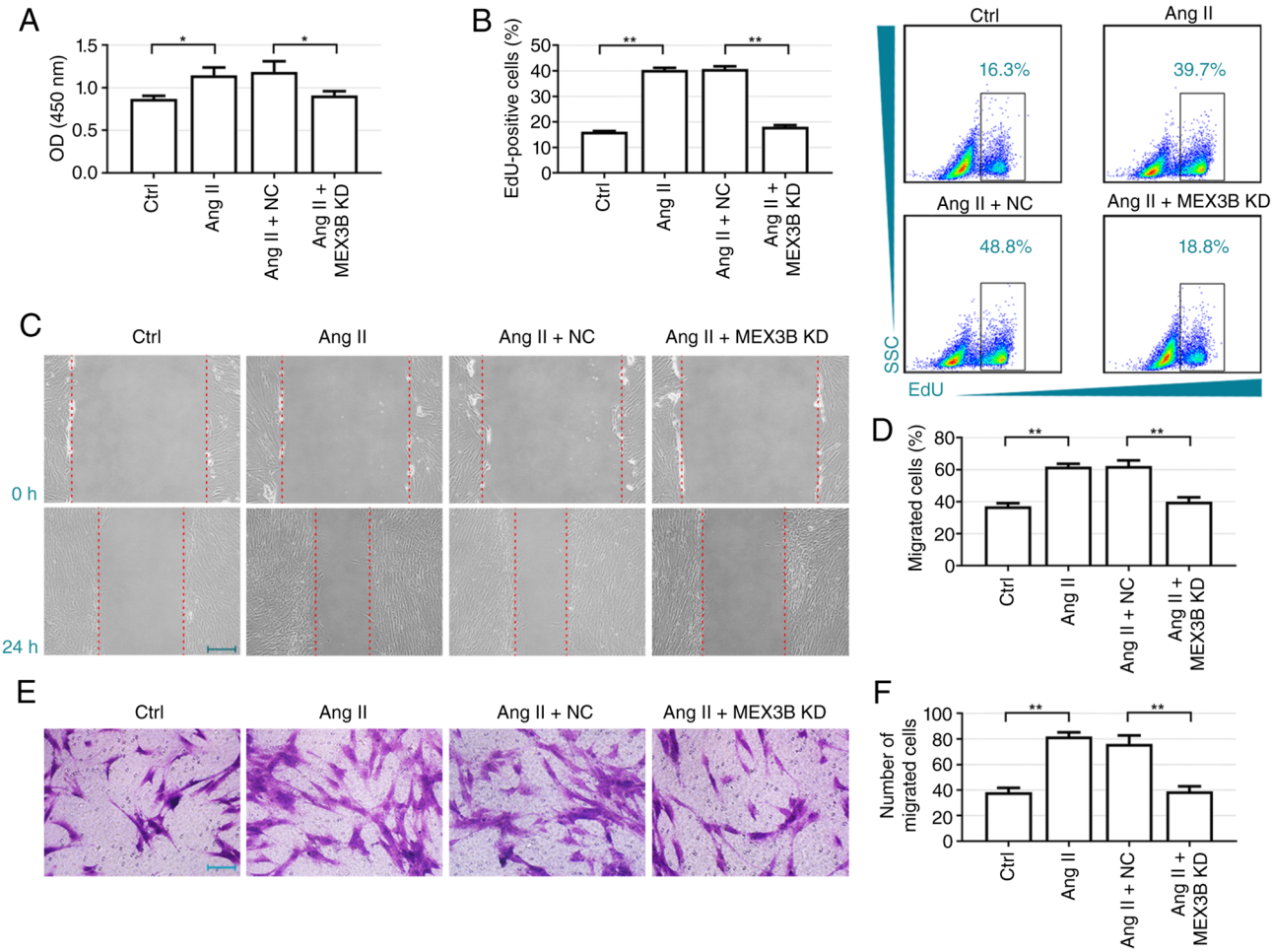


Figure 5. MEX3B KD inhibits Ang II-induced phenotype switching of VSMCs. (A) Cell viability was measured using a Cell Counting Kit-8 assay. (B) Cell proliferation was evaluated by EdU staining. (C) Cell migration ability was assessed by wound healing (scale bar, 200 μm) (D) Migrated cells by wound healing. (E) Transwell assay (scale bar, 100 μm). (F) Migrated cells by Transwell assay. n=3. *P<0.05; **P<0.01. Ang II, angiotensin II; α-SMA, α-smooth muscle actin; MEX3B, mex-3 RNA binding family member B; VSMC, vascular smooth muscle cell; KD, knockdown; OD, optical density; Ctrl, control; NC, negative control; SSC, side scatter.

VSMCs, leading to the upregulation of MEX3B (Fig. 7E). Dual-luciferase reporter assay was performed using a vector expressing an RNA-binding deficient MEX3B mutant (MEX3B mutKH), in which key residues that participate in RNA binding, including G177 and G83 in KH domains, are replaced with D. MEX3B overexpression-induced elevated relative luciferase activity was decreased by MEX3B mutKH (Fig. 7F). Whether MEX3B control the mRNA stability of VCAN was investigated. Following actinomycin D treatment, VCAN mRNA levels declined in a time-dependent manner, with a faster decay upon MEX3B knockdown and a slower decay following MEX3B overexpression (Fig. 7G). These data suggested that MEX3B potentiates VCAN mRNA stability.

RNA-binding-deficient MEX3B fails to regulate the phenotype transformation of VSMCs. The present study assessed whether the effects induced by MEX3B were dependent on its RNA-binding functions. MEX3B overexpression induced the upregulation of VCAN, whereas the expression of VCAN was not changed by MEX3B mutKH (Fig. 8A). The upregulation of MEX3B induced the synthetic phenotype of VSMCs in the presence of Ang II, as evidenced by the downregulation of SM-MHC and the upregulation of OPN (Fig. 8B and C), as well as the enhanced cell viability and migration (Fig. 8D and E). The ELN levels were decreased in VSMCs with MEX3B overexpression (Fig. 8F). These phenotypes were not significantly changed by MEX3B mutKH (Fig. 8B-F). The data indicated that MEX3B regulates the phenotype transformation of VSMCs in an RNA-binding-dependent manner.

VCAN KD inhibits the Ang II-induced VSMC phenotype transformation. As loss of MEX3B blocked the abnormal VSMC phenotype switching, VCAN might serve a similar role as the downstream RNA substrates of MEX3B. siRNAs targeting VCAN were synthesized and transfected into VSMCs, resulting in the downregulation of VCAN (Figs. 9A and B and S1B). VCAN KD inhibited the Ang II-induced VSMC phenotype transformation, as evidenced by the upregulation of SM-MHC and downregulation of OPN (Fig. 9C). The concentration of ELN was increased by loss of VCAN (Fig. 9D). The proliferative and migratory abilities were suppressed by VCAN depletion (Fig. 9E and F).

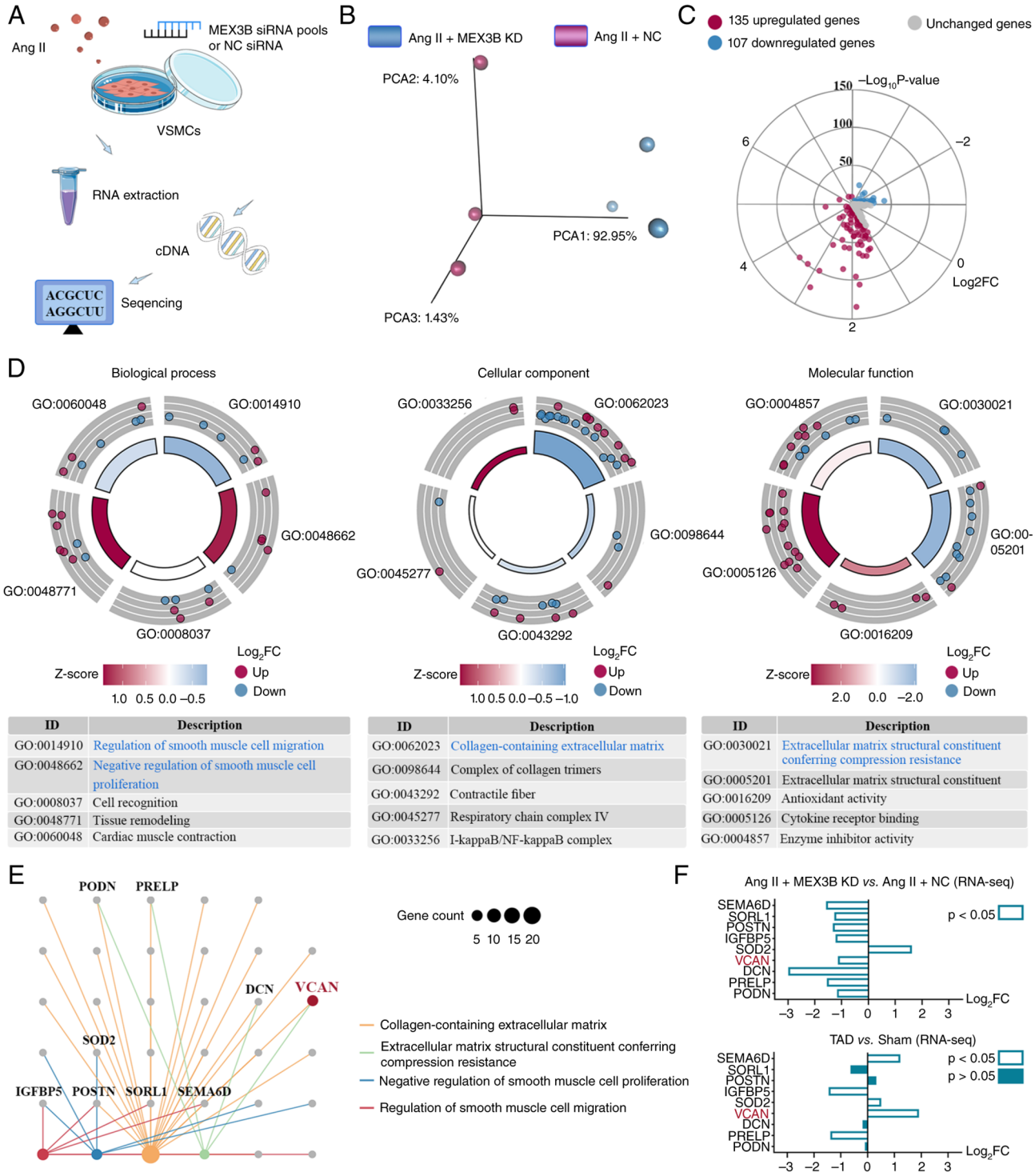


Figure 6. Downstream targets of MEX3B. (A) Experimental protocol for RNA-sequencing. (B) PCA was used to identify the samples from Ang II + NC and Ang II + MEX3B KD. (C) Volcano plot of differentially expressed genes ($|log_2FC|>1$; $P<0.05$). (D) GO enrichment analysis of the differentially expressed genes. (E) Association between functional terms and downstream factors of MEX3B. (F) mRNA expression according to RNA-sequencing. n=3. Ang II, angiotensin II; MEX3B, mex-3 RNA binding family member B; KD, knockdown; PCA, principal components analysis; NC, negative control; FC, fold-change; GO, Gene Ontology; si, small interfering; VSMC, vascular smooth muscle cell; TAD, thoracic aortic dissection.

Discussion

The present study found that MEX3B downregulation prevented the transformation of VSMCs to a synthetic phenotype, thus inhibiting TAD formation and deterioration. MEX3B promoted mRNA stability of VCAN by binding its 3'UTR. VCAN exhibited similar effects on VSMC phenotypic switching. The effects of MEX3B depletion on VSMC phenotype switch may be associated with the loss of VCAN (Fig. 10). Based on these findings, MEX3B signaling, which may be involved in regulating VSMC behavior, represents a promising subject for mechanistic studies, although its therapeutic applicability for TAD awaits verification.

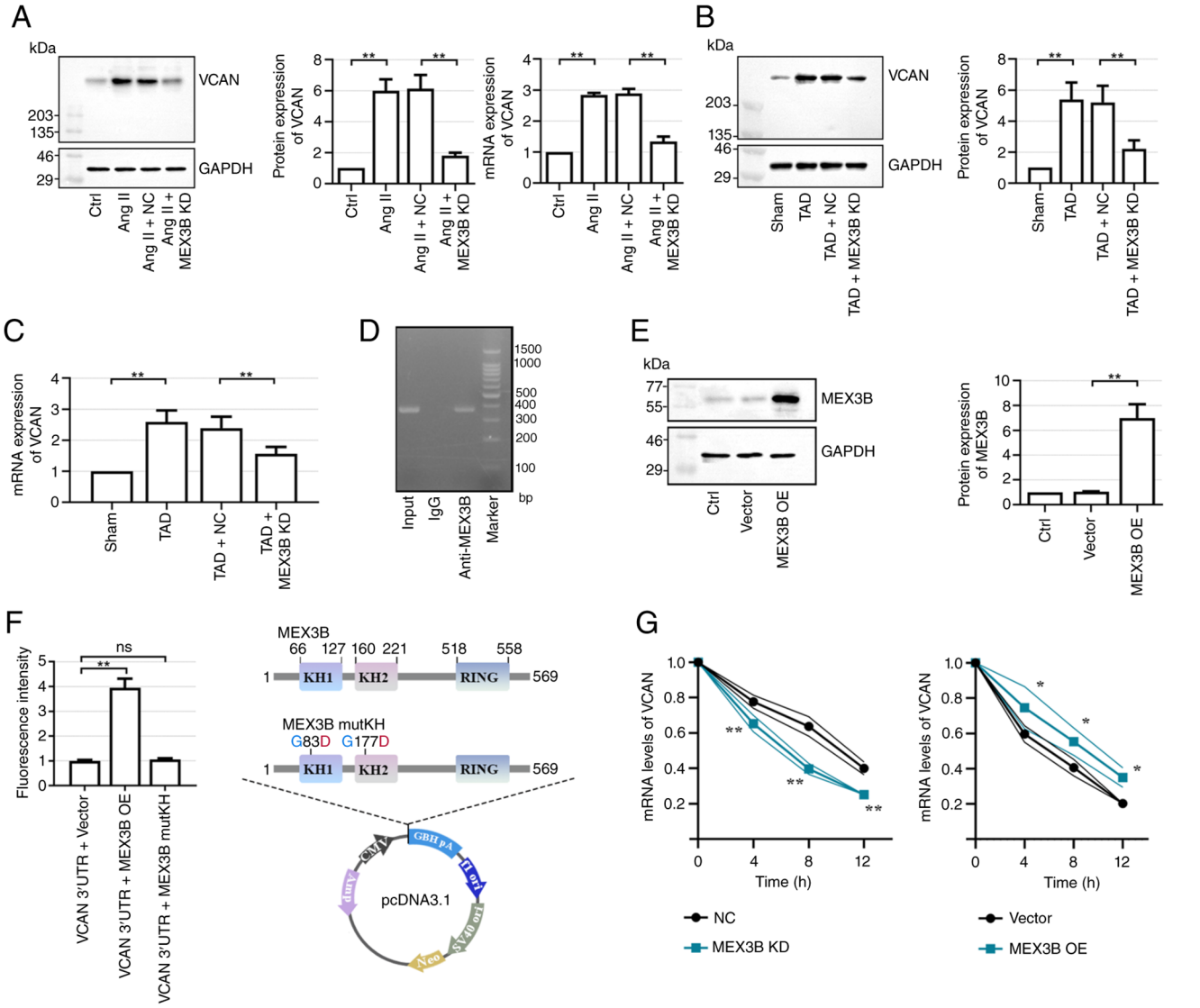


Figure 7. MEX3B potentiates VCAN mRNA stability. (A) mRNA and protein expression of VCAN in VSMCs with MEX3B KD in the presence of Ang II. (B) Protein and (C) mRNA expression of VCAN in aortic tissue of TAD mice with MEX3B KD. (D) Binding of MEX3B to VCAN 3'UTR was evaluated by RNA immunoprecipitation-PCR. (E) Protein expression of MEX3B by western blot in VSMCs transfected with MEX3B OE vectors. (F) Dual-luciferase reporter assay was performed using a pmirGLO containing the 3'UTR of VCAN mRNA and pcDNA3.1 containing wild-type MEX3B or MEX3B mutKH. (G) mRNA expression of VCAN in VSMCs treated with 10 μg/ml actinomycin D. n=3. *P<0.05; **P<0.01. ns, not significant; Ang II, angiotensin II; MEX3B, mex-3 RNA binding family member B; VCAN, versican; VSMC, vascular smooth muscle cell; KD, knockdown; TAD, thoracic aortic dissection; UTR, untranslated region; Ctrl, control; NC, negative control; OE, overexpression.

MEX3B is involved in the progression of multiple types of disease. For example, Liu *et al* (45) demonstrated that MEX3B is expressed in epithelial cells and exhibits pro-inflammatory properties in chronic rhinosinusitis. MEX3B participates in the differentiation state of neuronal progenitors (16). However, the role of MEX3B in TAD remains unclear. In the present study, interfering in MEX3B expression in VSMCs decreased TAD and ameliorated the degradation of ELN in the aorta. The stability and composition of the extracellular matrix is imperative for the maintenance of mechanical properties of the aorta (46,47). Enhanced elastic fiber degradation and upregulation of MMPs are observed in TAD, causing elevated aortic stiffness and decreased elasticity of aortic wall (46,48). MMPs are produced by synthetic VSMCs and MMP2 degrades the ELN and collagen (49,50). In the present study, the loss of MEX3B decreased the levels of MMP2, MMP9 and ELN in VSMCs induced by Ang II. The results were consistent with the phenotypic switch towards the contractile phenotype of VSMCs with MEX3B downregulation. Notably, MEX3B is an RNA-binding protein that binds the 3'UTR of other mRNAs and upregulates or downregulates their expression (51,52). In the present study, the RNA-binding function of MEX3B was responsible for the upregulation of genes containing the VCAN 3'UTR, as evidenced by increased relative luciferase activity in MEX3B-overexpressing cells and no marked changes in cells expressing the MEX3B mutKH mutant in the dual-luciferase assay. In addition, the synthetic phenotype of VSMCs induced by Ang II was not significantly changed by the transfection of MEX3B mutKH, indicating that MEX3B regulated the phenotype switching of VSMC in an RNA-binding-dependent manner. The function of MEX3B mutKH construct on VSMC phenotype switch was supported *in vitro* but not validated *in vivo*.

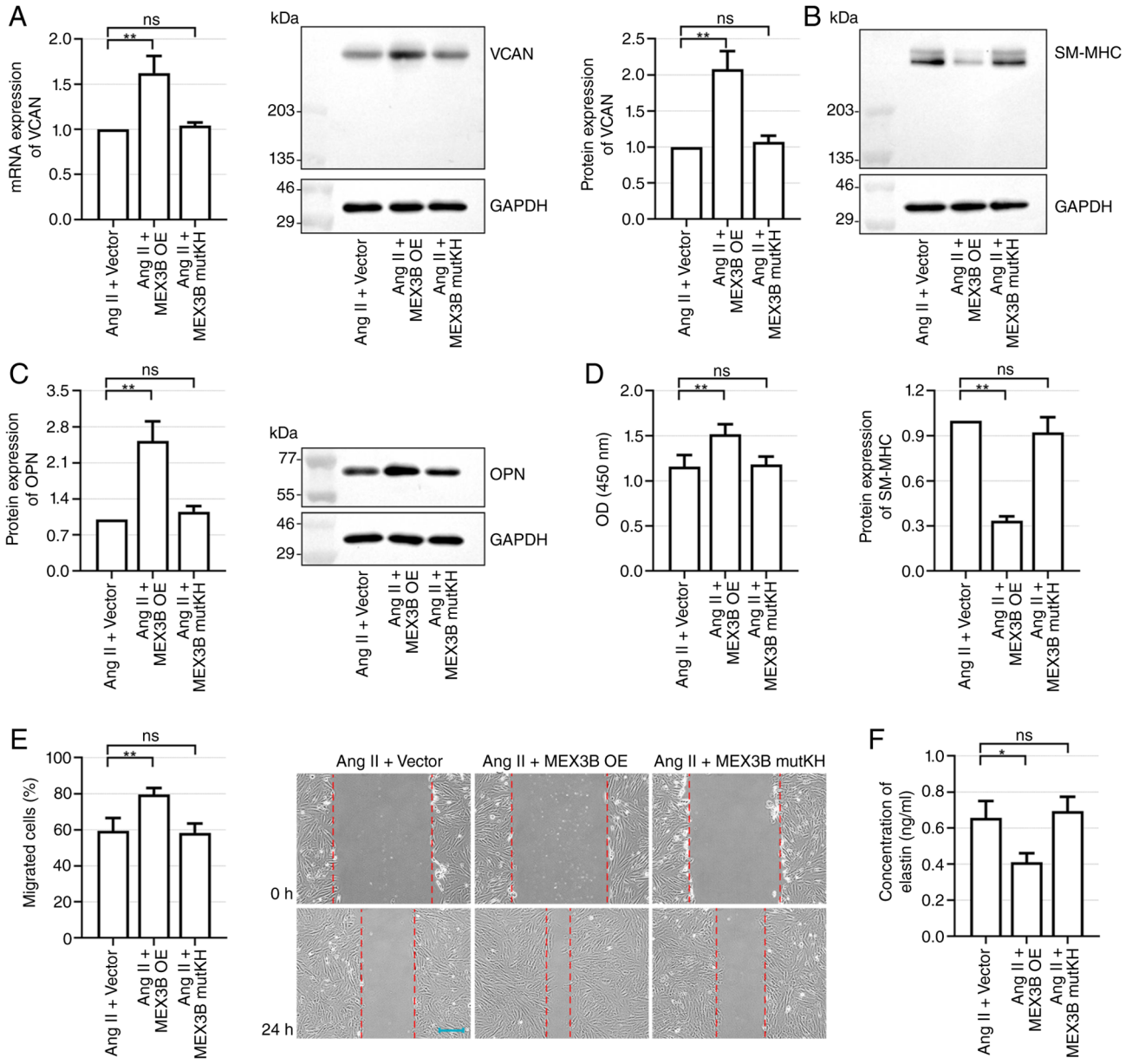


Figure 8. MEX3B regulates the phenotype transformation of VSMCs in an RNA-binding-dependent manner. (A) mRNA and protein expression of VCAN in VSMCs transfected with MEX3B-OE vectors or MEX3B mutKH. Protein expression of (B) SM-MHC and (C) OPN. (D) Cell viability was assessed by Cell Counting Kit-8 assay. (E) Cell migratory ability was measured by wound healing assay. Scale bar, 200 μm. (F) Concentration of elastin in cell supernatant. *P<0.05; **P<0.01. ns, not significant; Ang II, angiotensin II; MEX3B, mex-3 RNA binding family member B; OPN, osteopontin; SM-MHC, smooth muscle myosin heavy chain 11; VCAN, versican; VSMC, vascular smooth muscle cell; OE, overexpression; OD, optical density.

VCAN is a chondroitin sulfate proteoglycan. Under physiological conditions, VCAN contributes to the transmural distribution of residual stress in the aorta and normalizes the tensile stress across the wall (53). The pathological accumulation of VCAN in the aorta increases interstitial swelling pressure, leading to mechanical disruption of the extracellular matrix and media delamination (54). In the present study, VCAN was upregulated in the aortic wall of mice with TAD, as demonstrated by RNA-seq. As a downstream factor of MEX3B, VCAN may serve a role in TAD. Notably, the deficiency of VCAN inhibited the Ang II-induced VSMC synthetic phenotypic transformation, which is in line with a previous study (44). VCAN is upregulated in the medial layer of the aorta in patients with TAD compared with controls (54). As an upstream regulator of VCAN, it was hypothesized that MEX3B is upregulated in the TAD aorta, which was confirmed by bioinformatics analysis of the GEO dataset.

In the present study, the VSMC model was derived from human cells, whereas the TAD model was established in mice. Human VSMCs used for *in vitro* mechanistic studies allow direct acquisition of molecular regulatory data relevant to human disease and avoids false-positive results caused by species differences. The mouse artery model was used for *in vivo* functional validation because mice are genetically manipulable and have well-established TAD models (18,55,56). VCAN KD reverses aortic dilation and medial degeneration in a mouse model (43). In rat VSMCs, VCAN KD suppresses the proliferative and migratory ability and increases deposition

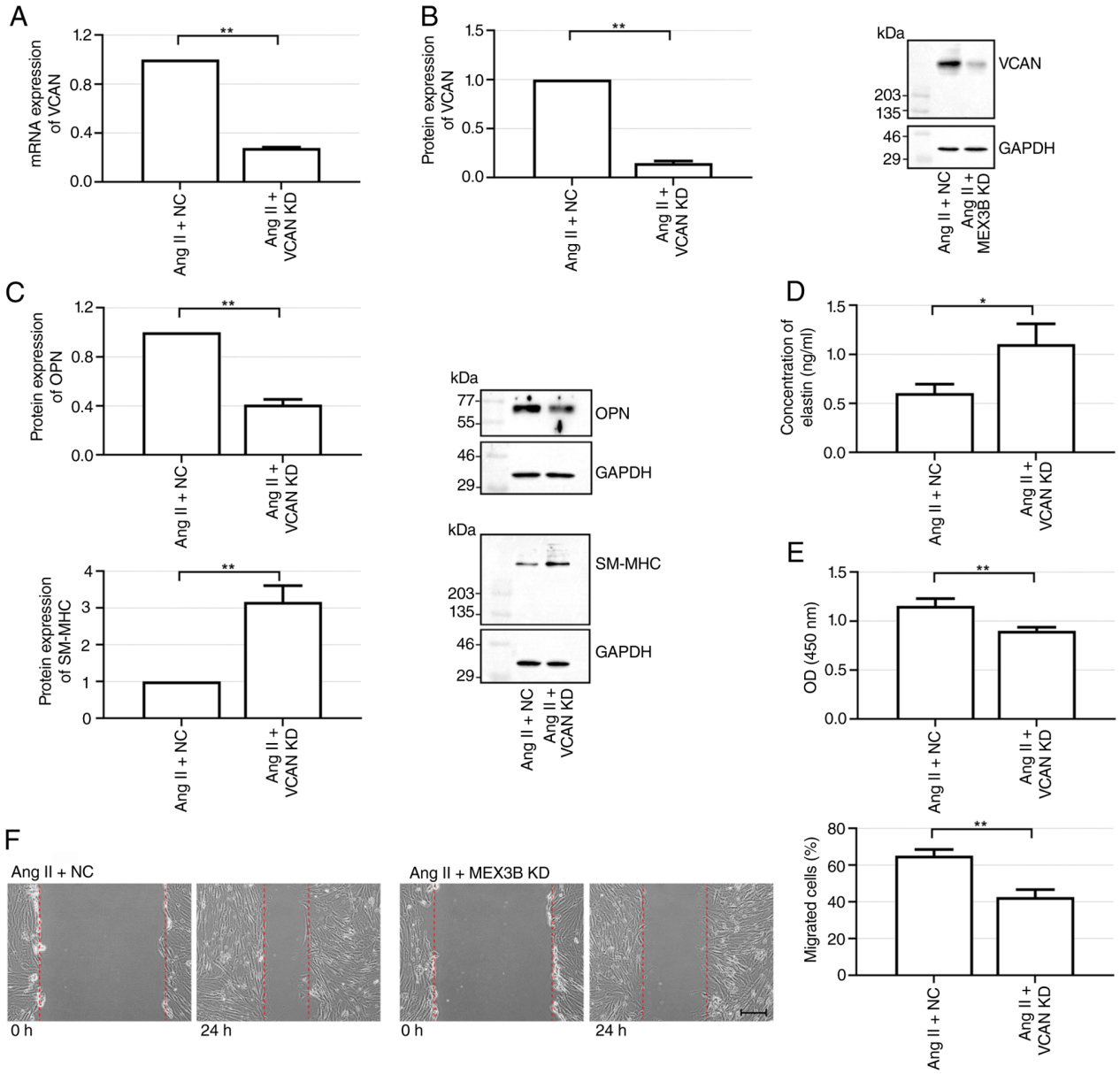


Figure 9. VCAN downregulation inhibits Ang II-induced VSMC phenotypic transformation. (A) mRNA and (B) protein expression of VCAN in VSMCs transfected with the VCAN siRNA pool in the presence of Ang II. (C) Protein expression of SM-MHC and OPN. (D) Concentration of elastin detected by ELISA. (E) Cell viability was evaluated by Cell Counting Kit-8 assay. (F) Cell migration was assessed by wound healing assay. Scale bar, 200 μm. n=3. *P<0.05; **P<0.01. Ang II, angiotensin II; MEX3B, mex-3 RNA binding family member B; VCAN, versican; VSMC, vascular smooth muscle cell; si, small interfering; SM-MHC, smooth muscle myosin heavy chain 11; OPN, osteopontin; KD, knockdown; NC, negative control; OD, optical density.

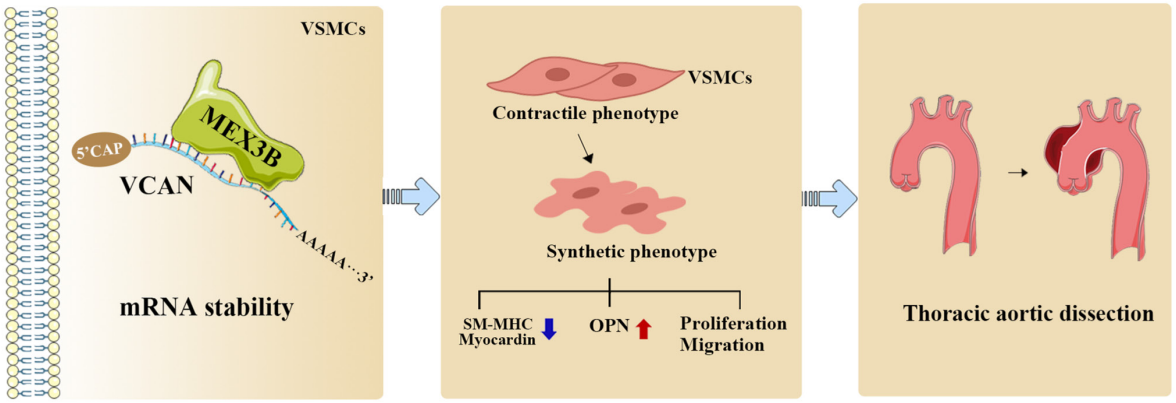


Figure 10. Potential underlying mechanism of MEX3B on aggravating thoracic aortic dissection. Ang II, angiotensin II; MEX3B, mex-3 RNA binding family member B; OPN, osteopontin; SM-MHC, smooth muscle myosin heavy chain 11; VCAN, versican; VSMC, vascular smooth muscle cell.

of elastic fibers (44). Similar results were shown in human VSMCs with VCAN KD in the present study, indicating that the function of VCAN might be conserved among species. In the present study, MEX3B upregulated VCAN expression in human VSMCs. TAD-induced upregulation of VCAN was decreased in aortic tissues of mice with MEX3B KD. The data suggest that the loss of MEX3B downregulated the expression of VCAN both in human VSMCs and murine aortic tissue of the TAD model.

In total, four transcripts of VCAN (V0, V1, V2 and V3) are produced due to the alternative RNA splicing of exons encoding GAG attachment domains. The VCAN V0 transcript contains GAGα and GAGβ domains. The V1 isoform has the GAGβ domain, and the V2 isoform has the GAGα, domain, while the V3 isoform has none (43). The V2 isoform is primarily expressed in the brain (57), and the V0/V1 isoforms are mainly expressed in VSMCs and fibroblasts of the developing heart (58). In TAD progression, VCAN V0 or V1 transcript KD inhibits the proliferation and migration of VSMCs, indicating the induction of a synthetic phenotype of VSMCs (44). However, the overexpression of the VCAN V3 transcript suppresses the proliferation and migration of VSMCs, as well as the production of ELN (59,60). It was hypothesized that the VCAN V0 isoform may serve a major role as a downstream factor of MEX3B in phenotypic transformation of VSMCs. Functional rescue experiments (overexpression of VCAN in MEX3B KD VSMCs or TAD models) should be performed to assess the regulation of MEX3B and VCAN. The coding DNA sequence (CDS) regions are V0 and V1 is 10,190 and 7,229 bp, respectively, which are too long to construct an overexpression vector. In the present study, MEX3B overexpression induced upregulation of VCAN, whereas the expression of VCAN was not changed by MEX3B mutKH. The function of MEX3B on TAD progression may be associated with the regulation of VCAN.

MEX3B exhibits RNA-binding function through the KH domain. The KH and RRM domain are the most common motifs in RNA binding proteins (41). According to the RNA-seq of aortas from TAD mice, 15 factors with RRM domains and two with KH domains were found. Notably, all factors with RRM or KH domains were upregulated in aortic tissue of TAD mice compared with the sham group. The promoting effects of MEX3B on TAD and the function of the other 14 RNA-binding proteins should be investigated in the future. MEX3A serves a role in atherosclerosis (61). Heterogeneous nuclear ribonucleoprotein A1 induces cardiomyocyte formation by enhancing cardiomyocyte dedifferentiation (62). insulin like growth factor 2 mRNA binding protein 2 mediates ferroptosis of VSMCs during the progression of thoracic aortic aneurysm (63). RNA binding motif protein 3 reestablishes the VSMC phenotypic switch of Ang II stimulation *in vitro* and is associated with AD *in vivo* (39). The present results suggested that these RNA-binding proteins were associated with diseases of the cardiovascular system, indicative of the potential of the RNA-binding proteins, including MEX3B, as molecular candidates for further functional investigation of TAD.

VSMC phenotypic switching in TAD progression is a complex cell reprogramming process regulated by interconnected signaling networks. VCAN may induce the VSMC phenotypic switch by numerous downstream pathways. For example, VCAN silencing reduces aortic dilation and medial degeneration in Marfan syndrome mice via inhibition of the Akt pathway (43). The inhibition of Akt induces the contractile transform of VSMCs (64). It was hypothesized that the VSMC phenotypic switch regulated by VCAN may be associated with the Akt pathway. VCAN activates integrin β1 signaling in VSMCs (65), while integrin β1 KD facilitates VSMC contractile gene expression (9), indicating that integrin β1 signaling may be another downstream factor of the VCAN signaling.

There were limitations to the present study. Firstly, as the effects of MEX3B were dependent on its RNA-binding function *in vitro*, MEX3B may function *in vivo* through a similar mechanism. However, the role of MEX3B mutKH *in vivo* remains unknown. Secondly, MEX3B and VCAN were upregulated in the medial layer of aortas of patients with TAD compared with controls. The association between MEX3B/VCAN expression and TAD severity/prognosis in clinical samples should be investigated. Finally, mechanistic analysis was confined to the MEX3B-VCAN level, lacking verification of the downstream pathways. A multi-directional framework should be developed as the present study did not investigate what drives MEX3B upregulation in TAD. Uncovering the upstream signals would provide a more complete regulatory map. Based on the mechanistic and phenotypic data, pharmacological targeting of MEX3B presents a direction for future functional studies. Existing compounds with potential MEX3B-inhibitory effects should be tested in experimental TAD models; whether combined approaches yield additive effects warrants further preclinical investigation. As the present findings were primarily derived from bioinformatic analyses and lack validation in human tissue, translational application for TAD diagnosis or intervention remains speculative. Thus, the present study provides mechanistic insights rather than offering immediate clinical solutions.

Taken together, the present findings suggested that the loss of MEX3B protected against TAD, potentially through its contribution to VSMC phenotype switching, which may involve downregulation of VCAN.

Acknowledgements

Not applicable.

Funding

The present study was supported by the Medical Health Science and Technology Project of Zhejiang Provincial Health Commission, China (grant no. 2024KY1103).

Availability of data and materials

The data generated in the present study may be found in the NCBI GEO under accession number GSE315273 or at the following URL: ncbi.nlm.nih.gov/geo/query/acc.cgi?acc=GSE315273).

Authors' contributions

JH and BX conceived the study, designed and performed the experiments, analyzed data and wrote the manuscript. SW

conceived the study and analyzed data. FH conceived and supervised the study and edited the manuscript. All authors have read and approved the final manuscript. JH and BX confirm the authenticity of all the raw data.

Ethics approval and consent to participate

All animal experiments were reviewed and approved by The Laboratory Animal Welfare and Ethics Review Committee of Zhejiang University (Hangzhou, China) following The Guideline for the Care and Use of Laboratory Animals (approval no. 29060).

Patient consent for publication

Not applicable.

Competing interests

The authors declare that they have no competing interests.

References

1. Landenhed M, Engström G, Gottsäter A, Caulfield MP, Hedblad B, Newton-Cheh C, Melander O and Smith JG: Risk profiles for aortic dissection and ruptured or surgically treated aneurysms: A prospective cohort study. J Am Heart Assoc 4: e001513, 2015.
2. Evangelista A, Isselbacher EM, Bossone E, Gleason TG, Eusanio MD, Sechtem U, Ehrlich MP, Trimarchi S, Braverman AC, Myrmel T, *et al*: Insights from the international registry of acute aortic dissection: A 20-Year experience of collaborative clinical research. Circulation 137: 1846-1860, 2018.
3. Bossone E and Eagle KA: Epidemiology and management of aortic disease: Aortic aneurysms and acute aortic syndromes. Nat Rev Cardiol 18: 331-348, 2021.
4. Thompson RW: Detection and management of small aortic aneurysms. N Engl J Med 346: 1484-1486, 2002.
5. Leng S, Li H, Zhang P, Dang Z, Shao B, Xue S, Ning Y, Teng X, Zhang L, Wang H, *et al*: SGK1-Mediated vascular smooth muscle cell phenotypic transformation promotes thoracic aortic dissection progression. Arterioscler Thromb Vasc Biol 45: 238-259, 2025.
6. Carrel T, Sundt TM, von Kodolitsch Y and Czerny M: Acute aortic dissection. Lancet 401: 773-788, 2023.
7. Amabili M, Balasubramanian P, Bozzo I, Breslavsky ID and Ferrari G: Layer-specific hyperelastic and viscoelastic characterization of human descending thoracic aortas. J Mech Behav Biomed Mater 99: 27-46, 2019.
8. Wang X, LeMaire SA, Chen L, Shen YH, Gan Y, Bartsch H, Carter SA, Utama B, Ou H, Coselli JS and Wang XL: Increased collagen deposition and elevated expression of connective tissue growth factor in human thoracic aortic dissection. Circulation 114: I200-I205, 2006.
9. Wang Y, Dong CQ, Peng GY, Huang HY, Yu YS, Ji ZC and Shen ZY: MicroRNA-134-5p regulates media degeneration through inhibiting VSMC phenotypic switch and migration in thoracic aortic dissection. Mol Ther Nucleic Acids 16: 284-294, 2019.
10. Jadli AS, Ballasy NN, Gomes KP, Mackay CDA, Meechem M, Wijesuriya TM, Belke D, Thompson J, Fedak PWM and Patel VB: Attenuation of smooth muscle cell phenotypic switching by Angiotensin 1-7 protects against thoracic aortic aneurysm. Int J Mol Sci 23: 15566, 2022.
11. Glisovic T, Bachorik JL, Yong J and Dreyfuss G: RNA-binding proteins and post-transcriptional gene regulation. FEBS Lett 582: 1977-1986, 2008.
12. de Bruin RG, Rabelink TJ, van Zonneveld AJ and van der Veer EP: Emerging roles for RNA-binding proteins as effectors and regulators of cardiovascular disease. Eur Heart J 38: 1380-1388, 2017.
13. Blech-Hermoni Y and Ladd AN: RNA binding proteins in the regulation of heart development. Int J Biochem Cell Biol 45: 2467-2478, 2013.
14. Buchet-Poyau K, Courchet J, Le Hir H, Séraphin B, Scoazec JY, Duret L, Domon-Dell C, Freund JN and Billaud M: Identification and characterization of human Mex-3 proteins, a novel family of evolutionarily conserved RNA-binding proteins differentially localized to processing bodies. Nucleic Acids Res 35: 1289-1300, 2007.
15. Huang L, Malu S, McKenzie JA, Andrews MC, Talukder AH, Tieu T, Karpinets T, Haymaker C, Forget MA, Williams LJ, *et al*: The RNA-binding protein MEX3B mediates resistance to cancer immunotherapy by downregulating HLA-A expression. Clin Cancer Res 24: 3366-3376, 2018.
16. Garg K, Sharma G, Samaddar S and Banerjee S: The RNA binding ubiquitination ligase MEX3B regulates bFGF-dependent neuronal proliferation. bioRxiv, Jul 2, 2024 doi: 10.1101/2024.06.28.601280.
17. Yamazumi Y, Sasaki O, Imamura M, Oda T, Ohno Y, Shiozaki-Sato Y, Nagai S, Suyama S, Kamoshida Y, Funato K, *et al*: The RNA binding protein Mex-3B is required for IL-33 induction in the development of allergic airway inflammation. Cell Rep 16: 2456-2471, 2016.
18. Ren W, Liu Y, Wang X Jia L, Piao C, Lan F and Du J: β-Aminopropionitrile monofumarate induces thoracic aortic dissection in C57BL/6 mice. Sci Rep 6: 28149, 2016.
19. Aicher BO, Zhang J, Muratoglu SC, Galisteo R, Arai AL, Gray VL, Lal BK, Strickland DK and Ucuzian AA: Moderate aerobic exercise prevents matrix degradation and death in a mouse model of aortic dissection and aneurysm. Am J Physiol Heart Circ Physiol 320: H1786-H1801, 2021.
20. Forrester SJ, Booz GW, Sigmund CD, Coffman TM, Kawai T, Rizzo V, Scalia R and Eguchi S: Angiotensin II signal transduction: An update on mechanisms of physiology and pathophysiology. Physiol Rev 98: 1627-1738, 2018.
21. Shi J, Yu W, Liang C, Shi H, Cao D, Ran Y, Qiao H, Dong Z and Liu J: S100A4 is a key facilitator of thoracic aortic dissection. Int J Biol Sci 20: 29-46, 2024.
22. Jia LX, Zhang WM, Zhang HJ, Li TT, Wang YL, Qin YW, Gu H and Du J: Mechanical stretch-induced endoplasmic reticulum stress, apoptosis and inflammation contribute to thoracic aortic aneurysm and dissection. J Pathol 236: 373-383, 2015.
23. Wang Y, Zhao ZM, Zhang GX, Yang F, Yan Y, Liu SX, Li SH, Wang GK and Xu ZY: Dynamic autophagic activity affected the development of thoracic aortic dissection by regulating functional properties of smooth muscle cells. Biochem Biophys Res Commun 479: 358-364, 2016.
24. Zhao Z, Wang Y, Li S, Liu S, Liu Y, Yu Y, Yang F, Xu Z and Wang G: HSP90 inhibitor 17-DMAG effectively alleviated the progress of thoracic aortic dissection by suppressing smooth muscle cell phenotypic switch. Am J Transl Res 11: 509-518, 2019.
25. Zheng HQ, Rong JB, Ye FM, Xu YC, Lu HS and Wang JA: Induction of thoracic aortic dissection: A mini-review of β-aminopropionitrile-related mouse models. J Zhejiang Univ Sci B 21: 603-610, 2020.
26. Barrett T, Wilhite SE, Ledoux P, Evangelista C, Kim IF, Tomashevsky M, Marshall KA, Phillippy KH, Sherman PM, Holko M, *et al*: NCBI GEO: Archive for functional genomics data sets-update. Nucleic Acids Res 41: D991-D995, 2013.
27. Wang J, Liu J, Yang F, Sun Y, Chen J, Liu J, Sun T, Fan R, Pei F, Luo S, *et al*: GMRSP encoded by lncRNA H19 regulates metabolic reprogramming and alleviates aortic dissection. Nat Commun 16: 1719, 2025.
28. Schneider VA, Graves-Lindsay T, Howe K, Bouk N, Chen HC, Kitts PA, Murphy TD, Pruitt KD, Thibaud-Nissen F, Albracht D, *et al*: Evaluation of GRCh38 and de novo haploid genome assemblies demonstrates the enduring quality of the reference assembly. Genome 27:849-864, 2017.
29. Liu J, Li Q, Hu Y, Yu Y, Zheng K, Li D, Qin L and Yu X: The complete telomere-to-telomere sequence of a mouse genome. Science 386: 1141-1146, 2024.
30. Ashburner M, Ball CA, Blake JA, Botstein D, Butler H, Cherry JM, Davis AP, Dolinski K, Dwight SS, Eppig JT, *et al*: Gene ontology: Tool for the unification of biology. The gene ontology consortium. Nat Genet 25: 25-29, 2000.
31. Gene Ontology Consortium: The Gene Ontology knowledgebase in 2026. Nucleic Acids Res 54: D1779-D1792, 2026.
32. Kanehisa M, Furumichi M, Sato Y, Matsuura Y and Ishiguro-Watanabe M: KEGG: Biological systems database as a model of the real world. Nucleic Acids Res 53: D672-D677, 2025.
33. Subramanian A, Tamayo P, Mootha VK, Mukherjee S, Ebert BL, Gillette MA, Paulovich A, Pomeroy SL, Golub TR, Lander ES and Mesirov JP: Gene set enrichment analysis: A knowledge-based approach for interpreting genome-wide expression profiles. Proc Natl Acad Sci USA 102: 15545-15550, 2005.

34. Schmittgen TD and Livak KJ: Analyzing real-time PCR data by the comparative C(T) method. Nat Protoc 3: 1101-1108, 2008.
35. Faul F, Erdfelder E, Lang AG and Buchner A: G*Power 3: A flexible statistical power analysis program for the social, behavioral, and biomedical sciences. Behav Res Methods 39: 175-191, 2007.
36. de Winter JC: Using the Student's t-test with extremely small sample sizes. Pract Assess Res Eval 18: n10, 2013.
37. Sullivan GM and Feinn R: Using effect Size-or why the p value is not enough. J Grad Med Educ 4: 279-282, 2012.
38. Kilchert C, Sträßer K, Kunetsky V and Änkö ML: From parts lists to functional significance-RNA-protein interactions in gene regulation. Wiley Interdiscip Rev RNA 11: e1582, 2020.
39. Xie Y, Gao R, Gao Y, Dong Z and Ge J: 11S proteasome activator REGγ promotes aortic dissection by inhibiting RBM3 (RNA Binding Motif Protein 3) pathway. Hypertension 80: 125-137, 2023.
40. de Bruin RG, Rabelink TJ, van Zonneveld AJ and van der Veer EP: Emerging roles for RNA-binding proteins as effectors and regulators of cardiovascular disease. Eur Heart J 38: 1380-1388, 2017.
41. Lorković ZJ and Barta A: Genome analysis: RNA recognition motif (RRM) and K homology (KH) domain RNA-binding proteins from the flowering plant Arabidopsis thaliana. Nucleic Acids Res 30: 623-635, 2002.
42. Jana S, Hu M, Shen M and Kassiri Z: Extracellular matrix, regional heterogeneity of the aorta, and aortic aneurysm. Exp Mol Med 51: 1-15, 2019.
43. Ruiz-Rodríguez MJ, Oller J, Martínez-Martínez S, Alarcón-Ruiz I, Toral M, Sun Y, Colmenar Á, Méndez-Olivares MJ, López-Maderuelo D, Kern CB, *et al*: Versican accumulation drives Nos2 induction and aortic disease in Marfan syndrome via Akt activation. EMBO Mol Med 16: 132-157, 2024.
44. Huang R, Merrilees MJ, Braun K, Beaumont B, Lemire J, Clowes AW, Hinek A and Wight TN: Inhibition of versican synthesis by antisense alters smooth muscle cell phenotype and induces elastic fiber formation in vitro and in neointima after vessel injury. Circ Res 98: 370-377, 2006.
45. Liu JX, Liao B, Yu QH, Wang H, Liu YB, Guo CL, Wang ZC, Li ZY, Wang ZZ, Ruan JW, *et al*: The IL-37-Mex3B-Toll-like receptor 3 axis in epithelial cells in patients with eosinophilic chronic rhinosinusitis with nasal polyps. J Allergy Clin Immunol 145: 160-172, 2020.
46. Wang L, Zhang J, Fu W, Guo D, Jiang J and Wang Y: Association of smooth muscle cell phenotypes with extracellular matrix disorders in thoracic aortic dissection. J Vasc Surg 56: 1698-1709. e1, 2012.
47. Wu D, Shen YH, Russell L, Coselli JS and LeMaire SA: Molecular mechanisms of thoracic aortic dissection. J Surg Res 184: 907-924, 2013.
48. Wagenseil JE, Nerurkar NL, Knutsen RH, Okamoto RJ, Li DY and Mecham RP: Effects of elastin haploinsufficiency on the mechanical behavior of mouse arteries. Am J Physiol Heart Circ Physiol 289: H1209-H1217, 2005.
49. Ishii T and Asuwa N: Collagen and elastin degradation by matrix metalloproteinases and tissue inhibitors of matrix metalloproteinase in aortic dissection. Hum Pathol 31: 640-646, 2000.
50. Borges LF, Touat Z, Leclercq A, Zen AA, Jondeau' G, Franc B, Philippe M, Meilhac O, Gutierrez PS and Michel JB: Tissue diffusion and retention of metalloproteinases in ascending aortic aneurysms and dissections. Hum Pathol 40: 306-313, 2009.
51. Takada H, Kawana T, Ito Y, Kikuno RF, Mamada H, Araki T, Koga H, Asashima M and Taira M: The RNA-binding protein Mex3b has a fine-tuning system for mRNA regulation in early Xenopus development. Development 136: 2413-2422, 2009.
52. Yamazumi Y, Sasaki O, Suyama-Fuchino S, Kohu K, Kamoshida Y, Harada H, Fujio K, Oda T and Akiyama T: The RNA-binding protein Mex-3B plays critical roles in the development of steroid-resistant neutrophilic airway inflammation. Biochem Biophys Res Commun 519: 220-226, 2019.
53. Azeloglu EU, Albro MB, Thimmappa VA, Ateshian GA and Costa KD: Heterogeneous transmural proteoglycan distribution provides a mechanism for regulating residual stresses in the aorta. Am J Physiol Heart Circ Physiol 294: H1197-H1205, 2008.
54. Cikach FS, Koch CD, Mead TJ, Galatioto J, Willard BB, Emerton KB, Eagleton MJ, Blackstone EH, Ramirez F, Roselli EE and Apte SS: Massive aggrecan and versican accumulation in thoracic aortic aneurysm and dissection. JCI Insight 3: e97167, 2018.
55. Zhao K, Zhu H, He X, Du P, Liang T, Sun Y, Jing Z and Zhou J: Senkyunolide I ameliorates thoracic aortic aneurysm and dissection in mice via inhibiting the oxidative stress and apoptosis of endothelial cells. Biochim Biophys Acta Mol Basis Dis 1869: 166819, 2023.
56. Anzai A, Shimoda M, Endo J, Kohno T, Katsumata Y, Matsuhashi T, Yamamoto T, Ito K, Yan X, Shirakawa K, *et al*: Adventitial CXCL1/G-CSF expression in response to acute aortic dissection triggers local neutrophil recruitment and activation leading to aortic rupture. Circ Res 116: 612-623, 2015.
57. Dours-Zimmermann MT, Maurer K, Rauch U, Stoffel W, Fässler R and Zimmermann DR: Versican V2 assembles the extracellular matrix surrounding the nodes of ranvier in the CNS. J Neurosci 29: 7731-7742, 2009.
58. Evanko SP, Angello JC and Wight TN: Formation of hyaluronan- and versican-rich pericellular matrix is required for proliferation and migration of vascular smooth muscle cells. Arterioscler Thromb Vasc Biol 19: 1004-1013, 1999.
59. Lemire JM, Merrilees MJ, Braun KR and Wight TN: Overexpression of the V3 variant of versican alters arterial smooth muscle cell adhesion, migration, and proliferation in vitro. J Cell Physiol 190: 38-45, 2002.
60. Merrilees MJ, Lemire JM, Fischer JW, Kinsella MG, Braun KR, Clowes AW and Wight TN: Retrovirally mediated overexpression of versican v3 by arterial smooth muscle cells induces tropoelastin synthesis and elastic fiber formation in vitro and in neointima after vascular injury. Circ Res 90: 481-487, 2002.
61. Santovito D, Henderson JM, Bidzhekov K, Triantafyllidou V, Jansen Y, Chen Z, Farina FM, Diagel A, Aslani M, Blanchet X, *et al*: Mex3a protects against atherosclerosis: Evidence from mice and humans. Circulation 150: 1213-1216, 2024.
62. Li C, Chen Y, Chen Q, Huang H, Hesse M, Zhou Y, Jin M, Liu Y, Ruan Y, He X, *et al*: RNA-Binding protein hnrnpa1 triggers daughter cardiomyocyte formation by promoting cardiomyocyte dedifferentiation and cell cycle activity in a Post-transcriptional manner. Adv Sci (Weinh) 12: e2402371, 2025.
63. Wang W, Chen J, Lai S, Zeng R, Fang M, Wan L and Li Y: METTL14 promotes ferroptosis in smooth muscle cells during thoracic aortic aneurysm by stabilizing the m6A modification of ACSL4. Am J Physiol Cell Physiol 328: C387-C399, 2025.
64. He W, Zheng Q, Zou T, Yan W, Gao X, Wang C and Xiong Y: Angiopoietin-like 4 facilitates human aortic smooth muscle cell phenotype switch and dysfunctions through the PI3K/Akt signaling in aortic dissection. Adv Med Sci 69: 474-483, 2024.
65. Zhu Z, Liu H, Feng L, Lu L, Zhu J, Liang Q, Lan Z, Ye Y, Wang S, Chen A and Yan J: Loss of ADAMTS5 promotes vascular calcification via versican/integrin β1/FAK signal. Atherosclerosis 404: 119190, 2025.

Copyright © 2026 Hong et al. This work is licensed under a Creative Commons Attribution-NonCommercial-NoDerivatives 4.0 International (CC BY-NC-ND 4.0) License.